

# Cold Dust in Early-Type Galaxies. I. Observations<sup>1</sup>

Pasquale Temi

*Astrophysics Branch, NASA/Ames Research Center, MS 245-6, Moffett Field, CA 94035;*  
*§ SETI Institute, Mountain View, CA 94043.*

Fabrizio Brighenti

*Dipartimento di Astronomia, Università di Bologna, via Ranzani 1, Bologna 40127, Italy;*  
*§ University of California Observatories/Lick Observatory, Board of Studies in Astronomy and*  
*Astrophysics, University of California, Santa Cruz, CA 95064.*

William G. Mathews

*University of California Observatories/Lick Observatory, Board of Studies in Astronomy and*  
*Astrophysics, University of California, Santa Cruz, CA 95064.*

Jesse D. Bregman

*Astrophysics Branch, NASA/Ames Research Center, MS 245-6, Moffett Field, CA 94035.*

## ABSTRACT

We describe far infrared observations of early-type galaxies selected from the ISO archive. This rather inhomogeneous sample includes 39 giant elliptical galaxies and 14 S0 (or later) galaxies. These galaxies were observed with the array photometer PHOT on-board the ISO satellite using a variety of different observing modes – sparse maps, mini-maps, over-sampled maps and single pointings – each of which requires different and often rather elaborate photometric reduction procedures. The ISO background data agrees well with COBE-DIRBE results to which we have renormalized our calibrations. As a further check, the ISO fluxes from galaxies at 60 and 100  $\mu\text{m}$  agree very well with those previously observed with IRAS at these wavelengths. The spatial resolution of ISO is several times greater than that of IRAS and the ISO observations extend out to 200  $\mu\text{m}$  which views a significantly greater mass of colder dust not assessable to IRAS. Most of the galaxies are essentially point sources at ISO resolution, but a few are clearly extended at FIR wavelengths with image sizes that increase with FIR wavelength. The integrated far infrared luminosities do not correlate with optical luminosities, suggesting that the dust may have an external, merger-related origin. In general the far infrared spectral energy distributions can be modeled with dust at two temperatures,  $\sim 43$  K

---

<sup>1</sup>Based on observations with ISO, an ESA project with instruments funded by ESA Member States (especially the PI countries: France, Germany, the Netherlands and United Kingdom) and with the participation ISAS and NASA

and  $\sim 20$  K, which probably represent limits of a continuous range of temperatures. The colder dust component dominates the total mass of dust,  $10^6 - 10^7 M_\odot$ , which is typically more than ten times larger than the dust masses previously estimated for the same galaxies using IRAS observations. For S0 galaxies we find that the optically normalized far-infrared luminosity  $L_{FIR}/L_B$  correlates strongly with the mid-infrared luminosity  $L_{15\mu\text{m}}/L_B$ , but that correlation is weaker for elliptical galaxies.

*Subject headings:* galaxies: elliptical and lenticular; galaxies: ISM; infrared: galaxies; infrared: ISM; ISM: dust, extinction;

## 1. Introduction

Most of our current knowledge of the infrared emission from elliptical galaxies is based on data from the *Infrared Astronomical Satellite* (IRAS) at 12, 25, 60 and  $100\mu\text{m}$  (Knapp et al. 1989). The IRAS satellite detected emission at all of these wavelengths from many bright elliptical galaxies, verifying the presence of dust in these galaxies having a wide variety of temperatures. Unfortunately, the spatial resolution of IRAS observations, 3 - 5' at  $100\mu\text{m}$ , is much larger than the optical size of most elliptical galaxies. Consequently, it has been impossible to disentangle various possible sources of dust emission. IRAS fluxes may confuse and combine emission from AGN, central dust clouds, circumstellar dust around red giant stars and truly interstellar dust distributed throughout the galactic volume. Worse, the large IRAS aperture may include irrelevant emission from other nearby sources.

Fortunately, the *Infrared Space Observatory* (ISO) (Kessler et al. 1996) has also detected many early-type galaxies at FIR wavelengths where emission from cold dust is expected to have its peak. The higher spatial resolution afforded by ISO is a necessary and essential attribute for a proper interpretation of infrared data from elliptical galaxies. ISOPHOT, the diffraction-limited imaging photometer on-board the ISO satellite (Lemke et al. 1996), also has a fainter limiting magnitude compared to IRAS and extends to somewhat longer wavelengths,  $200\mu\text{m}$ , permitting a better match to the cold dust emission expected from elliptical galaxies.

The origin of dust in elliptical galaxies is controversial. One confirmed source of dust is the collective outflow of dusty gas from evolving red giant stars. Emission attributed to circumstellar dust in E galaxies has been detected at  $\sim 10\mu\text{m}$  by Knapp et al. (1989) and Athey et al. (2002). A circumstellar origin seems secure since this emission shares the same de Vaucouleurs profiles with the optical images. As dusty gas moves away from orbiting red giants, it is eventually decelerated against the local hot interstellar gas,  $T \sim 10^7$  K, and subsequently undergoes a variety of complex gasdynamical interactions and instabilities. If the stellar dust grains ultimately come into contact with the hot interstellar gas, they would be eroded (sputtered) by thermal collisions with ions and destroyed in only  $\sim 10^7 - 10^8$  years. Nevertheless, during their relatively short lifetimes the grains absorb energy from starlight and incident thermal electrons and convert this energy to radiation

mostly at far infrared wavelengths (e.g. Tsai & Mathews 1995, 1996; Temi et al. (2003)). In this type of dust evolution we would expect that the metals contained in the dust grains would eventually merge with the hot interstellar gas and produce some of the observed X-ray line emission.

But this simple model for dust evolution does not take into consideration the highly efficient cooling that occurs when thermal electrons lose energy by inelastic collisions with dust grains. Mathews & Brighenti (2003) have recently argued that dusty gas ejected from stars may cool before or soon after entering the hot gas phase. The cooling rate of the hot dusty gas is dominated by emission from dust grains, not thermal X-ray emission. If this is the dominant evolutionary path for stellar dust, the thermal energy of the cooling ambient gas is emitted by the dust as far infrared emission. This type of rapid dust-induced cooling may create the dusty disks and clouds seen in the majority of luminous elliptical galaxies (e.g., van Dokkum & Franx (1995); Ferrari et al. (1999)).

While stellar winds are a certain source of dust in elliptical galaxies, many authors have suggested that mergers with dust-rich dwarf galaxies are in fact the dominant source of dust. One good argument in favor of an external source of dust in elliptical galaxies is the lack of any strong correlation between FIR and optical galactic luminosities (e.g. Forbes et al. (1991); Goudfrooij & de Jong (1995); Trinchieri & Goudfrooij (2002)). Further support for an external origin comes from counter-rotating warm gas observed in some elliptical galaxies (e.g. Caon et al. (2000)).

This is the first of a series of papers in which we shall explore and interpret archival ISO observations of early-type galaxies. In this paper we review the ISO observational data and describe the data reduction analysis used to retrieve the spatial location and emission spectrum of dust in these galaxies. In a subsequent paper we will use these data to investigate the origin, evolution, and physical properties of dust in early-type galaxies.

## 2. The sample

Working under the ISO Guest Investigator Programme, we searched the ISO archive to extract FIR data ( $\lambda \geq 60 \mu\text{m}$ ) for all the early-type galaxies observed with *ISOPHOT*. We excluded M86 from the sample because it has already been studied in detail by Stickel et al. (2003). No other selection criteria were used. All the far-IR data presented in this paper are unpublished except the data relative to NGC 3998 (Knapp et al. 1996). As expected from archival data, the sample is varied and somewhat inhomogeneous. Table 1 shows a detailed log of the *ISOPHOT* observations that we reduced and analyzed; entries in the table include for each source the coordinates, the ISO observation time identification number (TDT), the filter used, the observing mode, the field of view, the raster size when applicable and the total integration time. While most of the target galaxies in our sample have full coverage in wavelength from 60 to 200  $\mu\text{m}$ , some do not, depending on the particular scientific intentions of the original ISO PIs who requested the data.

The relevant properties of the sample galaxies are summarized in Table 2. The optical data

are taken from the Lyon-Meudon Extragalactic Database (LEDA; Paturel et al. (1997)) and the Revised Shapley-Ames (RSA) Catalog (Sandage & Tamman 1981). Of the 58 galaxies in Table 2, 43 are ellipticals and 15 are S0 or later types, according to RSA classifications. Most objects in the sample are optically luminous “giant” galaxies, which are our primary targets for this investigation. Table 2 also includes a few early-type dwarf galaxies (NGC 147, NGC 185, NGC 221, NGC 2328), defined here as galaxies with  $L_B \leq 10^9 L_{B,\odot}$ , that have been observed by ISO, but we do not include these galaxies in our final discussion. Since the evolution of interstellar dust in giant elliptical galaxies may be strongly influenced by its interaction with a hot interstellar medium (Tsai & Mathews 1995, 1996; Temi et al. (2003)), we also list in Table 2 the X-Ray luminosity  $L_x$ , taken from O’Sullivan et al. (2001), which is a measure of the amount of hot gas present in each galaxy. Only an upper limit to  $L_x$  is available for 24 objects. As expected from the well-known large scatter in the  $L_B - L_x$  relation for elliptical galaxies (e.g. Eskridge et al. (1995)), the galaxies in our sample also span a wide range of  $L_x$ . A few galaxies in our sample are fairly strong radio sources and many may harbor an AGN or have LINER optical spectra. As a measure of the non-thermal emission from these galaxies, we list in column 5 of Table 2 the 6 cm radio emission taken from the compilation of Roberts et al. (1991). Goudfrooij (1994) argues that the FIR emission from the vast majority of early-type galaxies is produced by cool dust, although a significant additional non-thermal component may be present in few objects (e.g., NGC 4261 and NGC 4494). To investigate the possible connection between the FIR emission and the presence of cold gas, we also quote the HI mass (or upper limit) taken mainly from Roberts et al. (1991) and the molecular ISM mass, both corrected for our assumed distance. In the final column of Table 2 we list some very schematic notes for each galaxy taken from the literature regarding the detection of dust in optical studies, the presence of warm emission line gas and the possible interaction of the galaxy with other nearby galaxies.

### 3. Observations

Of the large number of observing modes available for the ISOPHOT instrument (Klaas et al. 2002), most of the nearly 60 early-type galaxies in the ISO archive have been observed with the photometric far-infrared cameras, C100 and C200, using observing configurations described by PHT 37/39, PHT 22, and PHT 32, referred to as the Astronomical Observing Template (AOT). The C100 camera is used to observe at 60, 90, and 100  $\mu\text{m}$  and has a  $3 \times 3$  pixel format with a  $46''$  pixel scale. The C200 camera is used for observations at 150, 180 and 200  $\mu\text{m}$  and has a  $2 \times 2$  pixel format with a  $92''$  pixel scale.

Our ISO sample is the largest currently available sample of nearby early-type galaxies studied in the FIR up to 200  $\mu\text{m}$ . These observations, collected from scientific projects originally proposed by several PIs, certainly do not form a complete or homogeneous sample. Nevertheless, they have some statistical relevance and their maps represent the deepest FIR images acquired to date, achieving sensitivities an order of magnitude deeper than IRAS at 60 and 100  $\mu\text{m}$ . Also, ISOPHOT

observations taken in the oversampled map mode provide a spatial resolution far greater than the previous IRAS data. In a few cases the galaxies are resolved on scales comparable to their optical images, allowing a more trustworthy interpretation of their FIR emission.

The PHT 37/39 observational mode (AOT) produces sparse maps. These data were recorded in the on-off mode, where observations were made in each filter with one on-source single point staring mode and one off-source exposure. Eight galaxies in our sample have been observed in this observing mode. The 60 and 100 $\mu\text{m}$  filters were observed with C100 and 180 $\mu\text{m}$  with C200. Unfortunately, because of the limited field of view in the single pointing mode, some of the needed spatial information may be lost using this observing mode, but we were nevertheless able to perform some useful integrated photometry on the array with this AOT once the off-source has been subtracted.

A large fraction of the sample has been observed in the PHT 22 AOT, either in the mini-map configuration or in the on-off chopping mode. The PHT 22 mini-maps were made with a sequence of staring observations on a bidimensional regular spatial grid determined by spacecraft pointing. Data were recorded at each pointing position with the same detector settings. Eight galaxies were observed in the mini-map mode. All but one have been observed at 60, 90, 170, and 200  $\mu\text{m}$  with raster sizes of  $3 \times 3$  pixels for C100 and  $4 \times 2$  pixels for C200 in the  $Y \times Z$  direction. The final maps have sizes of  $4' \times 4'$  and  $7.5' \times 4.5'$ , respectively. For NGC1275 the only data available have larger raster maps ( $4 \times 4$ ) at 170 and 200  $\mu\text{m}$ . All measurements have been recorded with an integral number of pixel offsets, i.e., multiples of offsets by  $46''$  for the C100 array and  $92''$  for the C200 array. Of the recorded eight galaxies, only three were detected but these appear as point-like sources with no distributed galactic emission at the sensitivity level of the instrument.

Observations of 27 elliptical galaxies were made in the single pointing, multi-filter mode PHT 22. During each pointing, the focal plane chopper was used to alternate between exposures of the source and a reference field. Operating in a rectangular mode, the chopper has a throw of  $180''$  in the spacecraft Y-direction for both C100 and C200 cameras. Data was taken in four broad band filters centered at 60, 90, 170, and 200  $\mu\text{m}$ . The integration times for measurements at 60  $\mu\text{m}$  were 64 sec on-source and 64 sec off-source in four chopper cycles, while in the remaining three bands the time spent on and off source was 32 sec each. After the off-source subtraction, the photometry is acquired by summing the flux in the pixels.

The PHT 32 AOT observing mode uses a combination of raster mapping and chopper sweeping to create an oversampled map. These observations consist of a scan of  $N \times M$  steps in the Y and Z spacecraft coordinates respectively. At each spacecraft pointing position the focal plane chopper samples the sky in steps of 1/3 of the pixel size, which is  $15''$  at 60 and 100  $\mu\text{m}$  and  $30''$  at 150 and 200  $\mu\text{m}$ . The raster sampling interval in Y is set to a multiple of the chopper sampling interval, while the sampling in the Z direction is controlled entirely by the spacecraft raster sampling interval in Z. Depending on the step intervals chosen to construct the raster map, the linear scans from each detector pixel can be combined to achieve a sampling in the sky that approaches the Nyquist limit  $\Delta\Theta = 17''$  at 100  $\mu\text{m}$ . Using either the C100 or C200 array cameras, PHT 32 observations

can provide a sampling of  $15'' \times 23''$  and  $30'' \times 46''$  over the sampled field, respectively. Typically, the maps presented here were made with raster sizes large enough to detect, if present, any faint emission due to cold dust distributed throughout the galaxy. In addition, as the dimension of the spacecraft raster in the Z direction is increased, the on-source integration time also increases since one row of the C100 or C200 detector continuously scans through the source, thus sampling the same region multiple times. These large maps also help determine the appropriate flat field correction.

Recently many ISOCAM observations of mid-infrared dust emission from early-type galaxies have been published (Ferrari et al. (2002), Athey et al. (2002), Malhotra et al. (2000)). While we concentrate here on the far-infrared emission from cold dust, it is of interest to find possible correlations between  $L_{MIR}$  and  $L_{FIR}$  for galaxies detected in both bands. Many of the galaxies in our sample have been observed in staring mode with ISOCAM at mid-infrared wavelengths (CAM01 AOT). The images have been taken with the  $32 \times 32$  Si:Ga array camera at the pixel scale of  $6''$  in the LW3 ( $\lambda_{ref} = 14.3\mu m$ ), LW9 ( $\lambda_{ref} = 14.9\mu m$ ), and LW10 ( $\lambda_{ref} = 12.0\mu m$ ) filters. The LW10 filter has been designed to mimic the IRAS  $12\mu m$  filter bandwidth. LW3 and LW9 have similar central wavelength, but a  $\lambda / \delta\lambda = 3$  and 8, respectively. Each observation consists of a collection of exposures, each one taken with the target galaxy centered at several positions on the array. Two galaxies, NGC 4261 and NGC4636, have been observed in the MIR with a plate scale of  $3''/pix$ , while large raster maps have been made for NGC 4552 and IC 1459. In this paper we reduced and obtained photometry at  $15\mu m$  for a dozen early-type galaxies that have been detected by ISOPHOT.

## 4. Data Reduction

Although all data presented here have been recorded using only the two C100 and C200 far-infrared cameras, the data reduction process has to be specifically tailored for each AOT observing mode. In particular the detector response and flux calibration can be significantly different depending on the specific AOT employed. In the following we describe in some detail the data reduction procedure for each specific observing mode.

### 4.1. PHT 37/39 AOT

Data reduction and calibration were carried out using the ISOPHOT Interactive Analysis package (PIA) (Gabriel et al. 1997), together with the calibration data set V4.0 (Laureijs et al. 1998). The reduction included corrections for non-linearity, cosmic particle hits, and linear fitting of the signal ramps. After resetting all ramp slopes and subtracting the dark current, the detector responsivity was calibrated using measurements of the thermal fine calibration source (FCS) on-board. The sky-subtracted source signal was then corrected for the fraction of the point-spread

function not included in the field of view of the detectors. The error propagation in ISOPHOT data reduction is described by Laureijs & Klaas (1999). The statistical errors derived from signal processing are about 5-20 percent, depending on the wavelength range and object brightness, but systematic errors due to absolute calibration accuracy are estimated to be 30 percent (Klaas et al. 1998). As reported in the notes of Table 2, two galaxies, NGC 4105 and NGC 5353, appear to have companions that may be partially included in the beam and these companions may contribute to the detected flux (see below). Two galaxies, NGC 4291 and NGC 6876, were not detected at any of the three bands (60, 100, and 180  $\mu\text{m}$ ) observed.

#### 4.2. PHT 22 AOT mini-maps

All data have been processed using OLP version 10.1 and the reduction has been performed with PIA version 10.0. Data were corrected for non-linearity and cosmic particle hits. A linear fit is then applied to the ramps providing the signal per ramp data. A second cosmic ray hits correction was performed at this stage. Then all ramp signals are averaged over time at each raster point. At this stage the data are corrected for reset interval and the dark current is subtracted. A signal linearization is then applied to the data to correct for a changing response during the measurements.

The same reduction procedure is applied to the complementary measurements of the thermal FCS used to calibrate the fluxes. Two FCS observations are associated with each mini-map data set; one is recorded before and one after the source observation. An average of the two FCS measurements is converted to a real flux using tables constructed from sources for which the flux is well determined. After calibration the data are ready for mapping and the flux densities can be extracted.

Most of the galaxies in our sample are faint and, when detected, appear as point sources in the reduced maps. Uncertainties in the flux calibrations introduce errors of the order of 30 percent in the derived flux densities. The detection of a source, however, does not depend on the performance of the flux calibration, and the S/N ratio should be estimated before the flux calibration is performed. The raster maps constructed for these observations are well suited to derive the photometry of a point source. The central position is sampled nine times but enough data is available for background positions to make an accurate background subtraction.

Figure 1 shows the layout of the raster maps on the sky. Our observations have been constructed with raster steps equal to an integral number of pixels. This facilitates the derivation of flux densities from the maps since the correction factors for the point-spread function are only available for one-pixel intervals in both PHOT-C cameras. Under these conditions we are able to determine fluxes for each individual pixel. For both arrays the PSF is larger than one pixel, implying that each pixel at each raster position collects some emission from the central source plus background. The fraction of the central source flux allocated to each pixel in the array has been

estimated empirically by Laureijs (1999). Once the PSF correction is applied, the source and background flux densities can be extracted. Details concerning this reduction algorithm can be found in Richards & Klaas (2002) and Klaas et al. (2000).

### 4.3. PHT 22 AOT single-pointing

For single-pointing observations in the PHT 22 AOT we used PIA version 10.0, which includes all steps needed to fully process the raw data. Since this procedure is similar to our reduction of the PHT 22 mini-maps, we emphasize here the differences in the reduction process required in the single-pointing mode.

After correcting for non-linearity and cosmic particle hits, the on and off signals can be derived from the chopped measurements using the “Ramp Pattern” processing algorithm that uses a calibration table to correct for signal losses due to chopping. The first and last few readouts of each ramp were discarded since they are often affected by spurious electronic effects. Before deriving the signals, we inspected, and in some cases removed, part of the ramps that presented anomalies. We always discarded the first signal for chopper plateau since the detector response was not stabilized. The calibration of detector responsivity was performed using the associated measurement of the FCS. The source fluxes were corrected for transient effects and signal losses due to detector hysteresis in the chop cycle and the effect of vignetting on the illumination of the detector array. The accuracy of the absolute photometric calibration depends on systematic errors (Laureijs et al. 1998) and it is known to be better than 30 percent. Typical  $3\sigma$  noise limits for chopped observations were around 100 mJy and 150 mJy using the C100 and C200 detectors, respectively. The noise limits for regions observed with high interstellar cirrus confusion were a factor 3 or 4 higher than those with low cirrus emission.

### 4.4. PHT 32 AOT

These observations suffer from strong signal transients due to flux changes generated by the relatively fast chopper movement. To properly correct the data, we used procedures specifically developed for the PHT 32 AOTs by the MPI Kernphysik (Heidelberg) and supported by the ISO Data Center. These new procedures and routines have been recently incorporated into the standard PIA package (Gabriel et al. 1997), and are described in detail by Tuffs & Gabriel (2002). Here we briefly outline the most important steps taken in reducing the PHT 32 observations.

The ISOPHOT C200 Ge:Ga stressed array detector operating between 120 and  $200\mu\text{m}$ , and especially the C100 Ge:Ga array detector operating between 60 and  $100\mu\text{m}$  have complex non-linear responses. The non-linearities depend on the illumination history over timescales of 0.1-100 sec, on the absolute flux level and on the flux changes involved. Normally processed ISOPHOT data can be reduced in one pass from the raw input data with full time resolution to the final calibrated



map. To correct for responsivity drift effects, however, it is necessary to iterate between a sky map and the input data at full time resolution, and this has been implemented in the dedicated data reduction package.

The first basic step in reducing the PHT 32 mapping observations is signal conditioning. This procedure aims to provide a data timeline free of artifacts such as glitches, dark current, and non-linearity effects, but retains all knowledge of the transient response of the detector to the illumination history at the full time resolution of the input data. Signal conditioning is applied individually to each detector pixel. Also at this stage a rectangular grid of pointing directions on the sky, the *natural grid*, is defined with information collected from the spacecraft pointing history during the specific observation. The natural grid, defined by the combination of chopper sweeping and raster mapping, has pixels that are 15'' and 30'' wide in the spacecraft Y coordinate for the C100 and C200 array detectors, respectively. This oversampling performed by the PHT 32 observing mode becomes very useful when constructing maps of the surface brightness distribution of a sky field since it eliminates interpolation or any other map reconstructing techniques that often introduce artifacts in the final map. During signal conditioning, the data are corrected for nonlinearity effects in the integration ramp and dark current subtraction. A deglitching procedure is also applied to remove spikes in detector responsivity from cosmic rays hitting the array.

The second basic step in reducing PHT 32 maps is transient correction, an iterative process to determine the most likely sky brightness distribution giving rise to the observed signals. This is a nonlinear optimization problem. The sky brightness at each point in the predefined natural grid is the variable that is optimized iteratively by minimizing the difference between the input data and a combination of the detector response model with a trial data timeline. Since no theory exists to predict the detector response behavior, an empirical model has been found to apply the transient correction to the data. The severity of the data reduction difficulty depends on both the source/background ratio and the dwell time at each pointing direction. Because galaxies in our sample are not very bright, the transient corrections are not as large as those of bright compact sources, but they are nevertheless crucial to achieve the highest accuracy in the integrated photometry.

Before running the routines designed to reduce the PHT 32 data (P32tools), we processed the two FCS measurements taken before and after each raster observation, using the standard reduction with PIA. At first, once the P32tools package is started, the data are processed and corrected for ramps linearization, dark current subtraction and the reset interval correction. After this preliminary reduction the process become interactive and the chosen parameters are adjusted to each single observation. For the drift fitting procedure, we used the internal dispersion as the errors to be considered, and we included the slew data in the “coadded” or “sequence” option depending on the brightness of the object. The number of iterations of the starting condition and for the illumination history were left to their default values of 1 and 2 for the C100 and C200 arrays, respectively. At first the drift correction was applied for all detector pixels with the default fitting parameters. We inspected single pixels to see the need for modification of the drift fit and

also to apply a manual deglitching. Since most of the galaxies in the PHT 32 sample are faint, the deglitching procedure became critical and was applied regularly on a single pixel inspection basis. When the inspection of drift corrected map was satisfactory, we exported the results of the P32tools package to PIA. Once the transient correction has been applied to the observed signal, we proceeded to construct the final calibrated maps. For each galaxy we used the FCS measurements to convert the signal from detector units ( $V \ s^{-1}$ ) to  $mJy \ ster^{-1}$ . For each filter exposure, we averaged the detector responses of the two FCS measurements. Finally we applied the flat field correction assuming a uniform background emission.

#### 4.5. CAM 01 AOT

Data reduction has been performed using the Camera Interactive Analysis (CIA) package, version 5.0 (Ott et al. 1997). The procedure to reduce ISOCAM data starts with the dark current subtraction, for which we used the *model* option to take into account the long term drift in the dark current which occurred during the ISO mission. Then we removed the cosmic ray hits using a sigma clipping filter or multi-resolution method. This removes most of the short-term duration glitches. We also visually inspected the frames to manually remove glitches with very long time constants that may affect more than one frame. After the memory effects were corrected using the Fouks-Schubert method, we flat-fielded the data with library flat-fields. The conversion from electronic units to  $Jy/pix$  was performed using the standard CAL-G calibration data that accompanies the data products. The sky background was evaluated by taking the average pixel value from several blank regions in the reduced frames. After each single exposure has been properly reduced, the final image was produced by registering and coadding each frame.

### 5. Calibration Accuracy

In this section we compare the absolute calibrations of the ISO fluxes with those observed with other FIR instruments. The standard method of ISOPHOT flux calibration is to measure the fine calibration source (FCS), a greybody inside the ISOPHOT instrument. Using the mean of two FCS measurements recorded before and after each source observation, the signals are converted to surface brightness values in  $MJy \ sr^{-1}$ . The observed FCS flux is converted to a real flux using calibration tables constructed from observations of standard stars, planets and asteroids. We have cross-checked the ISO FCS-based calibrations by comparing the surface brightnesses of the backgrounds measured by C100 and C200 cameras with a background model based on COBE-DIRBE observations.

The background is estimated at each galaxy position by combining the contributions from the zodiacal light and Galactic emission. The zodiacal light emission depends on the ecliptic latitude  $\beta$  and the solar elongation  $e$ . Observing constraints for the ISO satellite have restricted most of

the observations to a range of solar elongation between  $60^\circ$  and  $120^\circ$ . This range in elongation is very similar to that of DIRBE ( $64^\circ - 124^\circ$ ) so both instruments sampled the same part of the solar system. The zodiacal contribution is based on models by Kelsall et al. (1998) and Reach (2000) in which the absolute brightness of the zodiacal light is normalized to the time variation of the sky brightness observed by COBE-DIRBE. At each position the DIRBE zodiacal light model takes into account emission from the three distinct dust components that constitute the model: a dust cloud that encompass most of the solar system, a dust ring around the sun at 1 AU, and dust bands from the asteroid families that extend from the asteroid belt to the sun. The thermal emission calculated by integrating the model along the line of sight is color-corrected before it is scaled to the resulting brightness.

The contribution to the background brightness from Galactic cirrus emission is based on a FIR map developed by Schlegel, Finkbeiner & Davis (1998). This map takes advantage of both the accurate calibration of the DIRBE FIR data and the higher angular resolution of the IRAS  $100\ \mu\text{m}$  map. The distribution of interstellar dust is highly irregular and patchy and there is no available analytical model for its emission. Consequently, we estimate the emission from interstellar dust at all ISOPHOT bands by scaling to the  $100\ \mu\text{m}$  map of Schlegel, Finkbeiner & Davis (1998), using a generic spectrum of the interstellar medium. The sky brightness is dominated by Galactic emission at all wavelengths measured with the C200 camera. The C100 60 and  $100\ \mu\text{m}$  data also have significant contributions from the interstellar cirrus emission, depending on the galactic latitude of the target galaxy.

We have derived and removed the background brightness at the celestial coordinates of each galaxy in our sample at the same epoch that the ISOPHOT measurements were taken. The PHT 32 oversampled maps were large enough to include a large number of "background" pixels that allowed us to properly evaluate the local sky brightness. The mini-maps have more limited spatial coverage, but the background flux was estimated using a standard method based on the determination of fluxes for each individual pixel as described in (Klaas et al. 2000). The single pointing measurements (PHT 37/39 and PHT 22) provide us with a well sampled background field recorded during the off-source pointing. All ISOPHOT background measurements were then color corrected according to a representative "average" spectral energy distribution (SED) of the two-component sky background model described above.

Figure 2 shows the color-corrected ISO backgrounds plotted against the color-corrected COBE-DIRBE measurements toward each galaxy in our sample. The mean ratios ISO/DIRBE for the color-corrected background responses are listed for each filter in Table 3. A very good correlation is seen between ISO and DIRBE backgrounds at all wavelengths; the scatter in the ISO/DIRBE ratio is within the uncertainty expected in the ISO absolute flux calibrations, and the dispersion of the data points is reasonably well distributed around the 1:1 line. The single-pointing observations (PHT 22 and PHT 37/39) show very little dispersion in the ISO/DIRBE ratios with average values confined within 6-7 percent for both the C100 and C200 cameras. The oversampled map observations show a slightly larger dispersion in the background ratios, particularly for measurements

taken at shorter wavelengths with the C100 detector. As seen in Figure 2 the PHT 32 data at 60, 90 and 100  $\mu\text{m}$  show systematic offsets from the 1:1 line by about 20 percent. In order to bring the ISO flux scale in line with the COBE-DIRBE flux scale, we divided each measurement by the appropriate factor shown in Table 3 prior to any further analysis. By this means we have normalized our measurements to the DIRBE flux scale. This also achieves a cross-calibration between the C100 and C200 detectors, since COBE-DIRBE has a spectral coverage that extends from 25 to 240  $\mu\text{m}$ . The adoption of the DIRBE flux scale also provides a common reference to calibrate the background response across all observing modes.

To further verify the absolute calibration of the ISO flux scale, we must show that the COBE-DIRBE normalization also results in accurate integrated fluxes for discrete sources. This was accomplished by comparing ISO and IRAS photometry for a number of elliptical galaxies in the two filters they have in common, 60 and 100  $\mu\text{m}$ . Although some ISO galaxies were resolved by ISOPHOT, we can safely consider them compact discrete sources since their extent is only slightly larger than the FWHM of the point-spread function of the two ISOPHOT array cameras. Calibrated survey scans from the IRAS satellite were extracted using the IRAS Scan Processing and Integration (SCANPI) software from IPAC. The software performs scan averaging of the IRAS raw survey data, applying several weighting methods for each coadded scan. The sensitivity gain, which depends on the local noise and number of scans crossing the target position, is a factor of 2-5 above the IRAS Point Source Catalog. In Figure 3 the integrated fluxes from 30 galaxies in the ISO sample (measured using the methods described in Section 6) are compared with IRAS fluxes at 60 and 100  $\mu\text{m}$ , revealing a good linear correlation between integrated flux densities.

## 6. Spatially Integrated Photometry

One goal of this work is to determine the integrated flux of each early type galaxy in the ISO sample and to improve upon earlier surveys of IRAS data. Both the increased ISOPHOT sensitivity and the higher spatial resolution can be exploited to improve the FIR fluxes. The method required to extract the integrated photometry depends on the ISO observing mode and the way the data have been acquired. About half of the ISO sample has been recorded in raster scans, either with PHT 32 oversampled maps or with the PHT 22 mini-maps mode.

The integrated photometry, listed in Tables 4, 5, 6, and 7, refers to flux densities that have not been color-corrected for background emission. When a color-correction is mentioned in the text, it refers to the correction applied to the fluxes under the assumption that the SED approximate a modified Planck curve ( $\beta=2$ ) with temperature 25 K.

**PHT 37/39 & PHT 22 single-pointing** - These observations collect emission from a single pointing in the sky through the  $2.3' \times 2.3'$  and  $3' \times 3'$  fields of view of the C100 and C200 cameras, respectively. The photometry was extracted using standard PIA procedures. Careful inspection of the C100 camera pixels was performed before adding the contribution of each individual pixel,

and, when appropriate, noisy pixels were discarded and not considered in deriving the source flux. Table 4 shows the photometric results along with the statistical error and background value for each of the galaxies observed in the PHT 37/39 mode. Table 5 lists the PHT 22 single-pointing photometry along with the errors and background values. A  $3\sigma$  value represents the upper limit to the flux of undetected galaxies.

**PHT 22 mini-maps** - We extracted integrated photometry for the eight galaxies observed in the mini-map mode using the algorithm incorporated into the PIA OLP V10 (Richards & Klaas 2002). The OLP V10 algorithms are appropriate for raster observations with a step size equal to the size of a pixel since the point-spread function corrections are defined for pixel separations in the two PHOT-C arrays. As expected, the photometric accuracy depends on the contrast between the source and the background flux. In general the mini-maps achieve considerably deeper photometry than IRAS with an absolute photometric accuracy better than 30 percent. Sources observed with the C200 array having fluxes less than about 0.1 Jy are not reliable. The derived fluxes are strictly accurate only for point sources, as required by the data fitting algorithm. If the source is extended, the derived flux could be underestimated by  $\sim 15\%$ , depending on its extension.

Five galaxies in the sample are not detected. However, even if the undetected galaxies are not point sources, we do not expect that the error in the upper limits derived with the OLP method is significant. For the three objects that show clear emission in the central position of the map, we carefully inspected the background pixels, and found no evidence for extended source emission; the photometry was then performed using the algorithm in PIA OLP V10. The background was evaluated as a weighted mean of all the pixels observed at various positions around the center of the map with oversampling rates of 6 and 4. Table 6 shows the flux densities and background flux values for the eight galaxies observed in this mode; column 3 and 5 show the flux densities and backgrounds derived using the PIA algorithm. The systematic errors, of the order of 30%, are larger than the statistical errors and are not included in the errors reported in Table 6.

**PHT 32 maps** - The integrated flux density can be determined from PHT 32 data by either integrating the maps after the background is subtracted or by integrating a model that best fits the data. Both methods have advantages and disadvantages. Integrations of the raw background-subtracted maps are very sensitive to the noise in the data and may severely affect the integrated photometry of low surface brightness objects. Furthermore, if any emission from the source is not covered during the scan, the derived photometry will be underestimated. However, it is very unlikely that incomplete scanning affects our photometry since the scans were large enough to sample the galaxies as seen in visual light down to about  $25 \text{ mag arcsec}^{-2}$ . Also, most spatially resolved detections with ISOPHOT are still quite compact in the infrared, extending only slightly beyond the FWHM of the instrumental PSF.

The model-fitting method can recover missing emission outside the maps, but it depends critically on finding parameters that properly describe the data. Such modeling also depends on the noise level in the maps and the spatial sampling on the sky. As mentioned in §4.1, the sampling

in the spacecraft Z-coordinate is lower than that in the Y-coordinate, making the determination of reliable parameters more uncertain. In Appendix we describe in detail the method used to extract the photometry with model fits.

Since it is unclear which method would be more accurate, we decided to derive integrated flux densities using both methods. The derived flux densities are listed in Table 7 where it is seen that there are no significant discrepancies between the direct integration and model-fitting methods. We adopted an empirical approach in evaluating the noise in the PHT 32 maps. Aperture photometry was performed on a number of independent areas spread over the map, avoiding any signal from the source. Our raster maps are always large enough to provide a significant number of pixels free from source emission. The measured scatter in the derived signal was used to estimate the noise in each map. For non-detections we derived upper limits to the flux density corresponding to the  $3\sigma$  noise level.

**CAM 01 maps** - We performed aperture photometry on the sky-subtracted frames. At 15  $\mu\text{m}$  the galaxies are resolved by ISOCAM, and some appear very extended. Since two galaxies have been observed with a smaller pixel scale of  $3''$ , we used an aperture of  $60''$  in radius to be consistent through all our sample. Table 8 shows the photometry in the mid-IR filters for the galaxies detected by ISOPHOT in a least one band.

## 7. Results

The ISOPHOT far-IR fluxes are presented in Tables 4, 5, 6 and 7. The far infrared emission from early-type galaxies is not large. Typical fluxes are in the range 0.1- 0.3 Jy at 60  $\mu\text{m}$  and 0.3 - 1.5 Jy at wavelengths up to 200  $\mu\text{m}$ . While FIR non-thermal emission from AGN in these galaxies can never be completely ruled out, many of the elliptical galaxies detected with ISO are rather radio-quiet and have FIR spectra that show no evidence of non-thermal source contamination. Nevertheless, when examined in detail many sample galaxies have peculiarities of some sort: an anomalously large amount of cold gas, indication of a recent merger or interaction with a companion, a counterrotating core, shells, etc. (see Table 2).

Of the 54 galaxies in our ISO sample (we exclude the four dwarf galaxies NGC 147, NGC 185, NGC 221, and NGC 2328 from this analysis), only 28 are detected in at least one ISO band at the  $3\sigma$  level, a detection rate of  $\sim 50$  percent. However, given the incompleteness of our sample, this detection rate may not be representative of early-type galaxies in general. In optical studies the dust detection rate for early-type galaxies is generally larger ( $\sim 80$  percent, van Dokkum & Franx (1995); Ferrari et al. (1999)). For the 39 elliptical galaxies in our sample, only 16 were detected by ISO ( $\sim 41$  percent), while for S0 and later types 11 out of 14 were detected ( $\sim 79$  percent). The detection rate is similar if we remove the known radio galaxies from the sample. Our detection rates for E and S0 galaxies are consistent with those found by Knapp et al. (1989) with a larger sample of early-type galaxies observed with the *IRAS* satellite ( $\sim 45$  and  $\sim 68$  percent for Es and

S0s respectively). Bregman et al. (1998) re-examined a subsample of the Knapp et al. (1989) IRAS galaxies in which peculiar galaxies, AGN and galaxies with possible observational problems were removed. Using this more limited subsample, they found a much lower detection rate of  $\sim 12$  percent. Most of the galaxies in their IRAS subsample also have rather large amounts of warm and cold gas.

In estimating the FIR emission from interstellar dust in elliptical galaxies, it is often assumed that the dust grains ejected from evolving stars are rapidly and widely dispersed into the hot interstellar gas (Temi et al. 2003). The dust then radiates the energy received by starlight and thermal electrons during the grain sputtering timescale. The predicted FIR emission from nearby giant E galaxies produced by this radiation model is just below the limiting flux observable with ISO. However, it may be more plausible that the dust ejected from the stars remains with the associated stellar gas as it is heated, producing a very inhomogeneous interstellar dust distribution (Mathews & Brighenti 2003). When the dust is locally more concentrated, the cooling of thermal electrons as they inelastically collide with dust grains can dominate over the usual thermal radiative cooling from the hot gas. Consequently, the FIR emission from the grains also includes the thermal energy of the hot ambient gas. If the total production of dusty gas by stellar mass loss in a large elliptical galaxy is  $\dot{M}$ , the maximum expected infrared emission is at least  $L_{FIR} \sim 5\dot{M}kT/2\mu m_p \sim 2 \times 10^{41} (T/10^7 \text{ K})(\dot{M}/M_\odot \text{ yr}^{-1}) \text{ erg s}^{-1}$ , where  $T$  is the (maximum) temperature of the hot dusty gas,  $\mu \sim 0.62$  is the molecular weight and  $m_p$  is the proton mass. For typical total mass loss rates from galactic stars,  $\dot{M} \sim 1 M_\odot \text{ yr}^{-1}$ , this is comparable to the FIR luminosities observed by ISO. Since  $\dot{M} \propto M \propto L_B$  and  $T \propto \sigma_*^2 \propto L_B^{1/2} \propto M^{1/2}$ , we would expect  $L_{FIR} \propto L_B^{3/2}$  on this emission model from galaxies with approximately constant stellar  $M/L_B$  and mean stellar age.

It has also been proposed that the majority of the ellipticals have acquired their dust by an accretion event (e.g. Forbes et al. (1991)). This possibility is supported by a comparison of the FIR and optical luminosities of the detected galaxies. In Figure 4 we plot  $L_B$  versus the FIR luminosity in the various ISO bands  $L_\lambda = F_\lambda \Delta_\lambda 4\pi D^2$ , where  $F_\lambda$  is the observed flux density at wavelength  $\lambda$ ,  $\Delta_\lambda$  is the bandwidth of the filter and  $D$  is the source distance. Since the emission in the various bands may be produced by dust with different origin, distribution, and temperature, we compared  $L_B$  with the luminosities in each FIR band, rather than use the total  $L_{FIR}$ . While one dust component might correlate with  $L_B$ , another may not. This, in principle, could reveal correlations between  $L_B$  and the emission of each dust component that could have been hidden if the integrated FIR luminosity was used. In Figure 4 we combine galaxies detected at 90 and 100  $\mu\text{m}$  (panel b) and galaxies detected at 150, 170 and 180  $\mu\text{m}$  (panel c), because of the large bandpass overlap of these filters. Elliptical galaxies are indicated with filled circles, S0 galaxies and later types are shown with open circles. No obvious correlation between  $L_B$  and any of the ISO band luminosities is evident (we verified that fluxes are also uncorrelated, as expected). This strongly suggests that the radiating dust is not associated with stellar mass loss but is more likely to have an external origin. On the other hand, Bregman et al. (1998) found a correlation  $L_{FIR} \propto L_B^{1.61}$  in their subsample of 15 elliptical galaxies with IRAS detections, which is similar to our predicted

variation for internally produced dust. They avoided peculiar galaxies, which may also introduce a random disturbance in the  $L_{\text{FIR}} - L_B$  relation.

The two galaxies in the uppermost left region of Figure 4, with very high  $L_{\text{FIR}}$  and relatively low  $L_B$ , are NGC 3928 and NGC 5666. These are very peculiar objects. NGC 3928 has an uncertain classification. Optically, it shows a small spiral feature embedded in an elliptical envelope. Its unusual blue colors and diffuse radio emission indicate starburst activity in the central region, possibly associated to the capture of a small dwarf galaxy by an otherwise normal elliptical galaxy (Taniguchi & Watanabe 1987). It has a large amount of cold gas ( $\gtrsim 5 \times 10^8 M_\odot$ ). NGC 5666 has also an uncertain morphology. The large FIR luminosity may come from dust associated with the very extended and massive HI envelope (Lake et al. 1987).

It is also interesting to compare the FIR and mid-infrared emission at  $\sim 15 \mu\text{m}$ . The mid-IR surface brightness is often distributed like the galactic stars (Knapp et al. (1992); Athey et al. (2002)), which has led to the identification of mid-IR with warm circumstellar dust recently ejected from evolving stars. Analyses of the integrated IRAS luminosity at  $12 \mu\text{m}$  reveal that  $L_{12\mu\text{m}}$  is roughly proportional to  $L_B$  (Jura et al. (1987); Eskridge et al. (1995)), although with significant scatter. In general, the mid-IR emission may have two components, one due to circumstellar dust which should be proportional to  $L_B$ , and one due to additional interstellar dust, possibly accreted.

To gain insight concerning the origin of the mid-IR, in Figure 5 we plot the “mid-IR excess”  $L_{15\mu\text{m}}/L_B$  against  $L_{\text{FIR}}/L_B$  for the galaxies detected at both  $15 \mu\text{m}$  and at least one of the ISO FIR bands. ISO data for  $L_{15\mu\text{m}}$  from Ferrari et al. (2002) have been added to the  $12 \mu\text{m}$  or  $15 \mu\text{m}$  data described in section 4.5. The  $L_{15\mu\text{m}}/L_B$  ratio is not constant among the galaxies, implying varying amounts of warm dust in some galaxies. While only a weak correlation of  $L_{15\mu\text{m}}/L_B$  with  $L_{\text{FIR}}/L_B$  is apparent among the elliptical galaxies, such a correlation becomes tighter for the S0 galaxies, pointing toward a common origin for the infrared enhancement in the mid and far infrared. Ellipticals seem to continue the correlation defined by the S0 galaxies at the faintest end of the IR emission, albeit with more scatter.

In Figure 6 we compare the FIR and X-ray luminosities for the subsample of ISO-detected galaxies with  $L_x$  listed in O’Sullivan et al. (2001). Upper limits for  $L_x$  are indicated with left-pointing triangles. If galaxies with very low  $L_x$  have less hot interstellar gas because of galactic outflows (e.g. Brown & Bregman (1998)), we might expect an anticorrelation between  $L_{\text{FIR}}$  and  $L_x$ , since grain sputtering by hot gas significantly reduces the dust emission (Tsai & Mathews 1995, 1996). However, no clear correlation is seen in our data. In the galactic merger hypothesis, the vertical scatter in Figure 6 might be interpreted as another manifestation of the random character of the dust accretion process. For galaxies in our sample with low  $L_x$ , a large fraction of the X-ray emission has a stellar origin. With this in mind, we also verified that  $L_{\text{FIR}}$  does not correlate with the *gas* X-ray luminosity, defined as the difference between the observed  $L_x$  and the collective X-ray luminosity from X-ray binaries assumed to be  $L_{x,\text{discr}} = 6 \times 10^{29} (L_B/L_{B,\odot}) \text{ erg s}^{-1}$  (e.g. Sarazin et al. (2001)).



We note that many galaxies with measured ISO emission show peculiarities indicative of galactic interactions or mergers. About half of the elliptical galaxies detected in the FIR also have large masses of cold gas (cf. Table 2), a rare property of ellipticals as a class. For several other ellipticals no data on the presence of cold ISM are available or the upper limits are not stringent. According to the usual interpretation, the cold gas has an external origin (e.g. Wiklind et al. (1995); Huchtmeier et al. (1995)). On average we find that galaxies that are luminous in the FIR also tend to have a large amount of cold gas, in agreement with Bregman et al. (1998).

### 7.1. Remarks on Galaxies with Companions

A few galaxies in the sample have a companion at small projected distance. For these objects the FIR flux may be contaminated by the presence of the companion. Below we briefly discuss the most relevant cases.

**NGC 2293** - This galaxy forms a pair with its interacting companion NGC 2292. The two galaxies, separated by about 0.8 arcmin, have very similar optical luminosities and morphologies. The ISOPHOT map is large enough to encompass the emission from the two galaxies, and the brightness distribution at 200  $\mu\text{m}$  is very extended and elongated in the axial direction connecting the two galaxies. Since the spatial resolution is not high enough to resolve each component, we suspect that the derived flux density takes contribution from both galaxies. The pair has not been detected at 60 and 100  $\mu\text{m}$ .

**NGC 4105** - This galaxy is strongly interacting with its nearby neighbor NGC 4106. Their angular separation 1.2' corresponds to a projected linear separation of only 12 kpc at a distance of 35 Mpc. The massive tidal arms in NGC 4106, very prominent in visible light, have evidently been pulled out by the encounter although no distortion of the elliptical isophotes is seen in NGC 4105 (Sandage & Bedke 1994). The pointing for the NGC 4105 ISO observation was accurately chosen to minimize the contribution to the flux from its companion. An overlap of the ISOPHOT-C field of view with an optical image of the target shows that the optical image of NGC 4106 lies outside the recorded field. Although we cannot accurately quantify the contribution of NGC 4106 to the FIR flux from NGC 4105, we do not expect it to be very significant.

**NGC 4649** - This galaxy is not detected in the far-infrared at any band, but its spiral companion, NGC 4647, is prominent at all three wavelengths. The angular resolution of the oversampled map nicely resolves NGC 4647. Located about 2' North-East of NGC 4649, this spiral companion is responsible for the high flux detection, which was erroneously attributed to the large elliptical in previous discussions of the IRAS observations. Our analysis of the optical and FIR images, shows that there is no FIR flux contribution from NGC 4649 (Temi et al. 2003).

**NGC 5353** - Photometry for this galaxy may also be slightly affected by its companion NGC5354, displaced 1.3' to the north. Both are early type galaxies. Although it is somewhat difficult to estimate, we do not expect NGC 5354 to contribute very much to the ISO FIR flux

observed for NGC 5353 because careful spacecraft pointing placed NGC5354 almost completely outside the detector beam.

Finally, two galaxies with companions, NGC 4291 and NGC 6876, were not detected at any of the three bands (60, 100, and 180  $\mu\text{m}$ ) observed.

## 7.2. Spectral Energy Distribution and Dust Temperature

The FIR spectral energy distributions (SEDs) for the galaxies detected by ISO are shown in Figure 7. The color-corrected ISOPHOT flux densities are shown with  $1\sigma$  errors. For all sample galaxies the SED peaks at wavelengths greater than 100  $\mu\text{m}$ , indicating the presence of a cold dust component that previous IRAS observations could not have detected.

Dust temperatures and masses can be derived by fitting modified blackbody functions to the SEDs. However, such fits may not be unique. The mass absorption coefficient  $k_\lambda$ , the exponent  $\beta$  of the dust emissivity,  $\epsilon_\lambda \propto \nu^\beta B_\nu(T_D)$ , and the number of dust components used in fitting the FIR data are all intervening factors in determining the goodness of the fit. Unfortunately, both  $k_\lambda$  and  $\beta$  are quite uncertain, and their values are still a matter of debate. As reported by Dunne & Eales (2001), Klaas et al. (2001), and Bendo et al. (2003), the FIR-submillimeter SEDs may be well fitted with different combinations of the emissivity index  $\beta$  and the number of dust temperature components used in the fit, so the interpretation is degenerate. Interpretations of the FIR SED are further complicated by our poor knowledge of the emissivity index  $\beta$ .

Most of our detected galaxies have four data points, probing the peak of the dust emission and the start of the Rayleigh-Jeans region. NGC 4261 has been observed in two different runs with both the PHT 32 and PHT 22 observing modes. A total of six FIR photometric points are available to constrain its temperature. While NGC 4261 is a strong radio source, there is no evidence of nonthermal emission at ISO wavelengths. For NGC 3557 fluxes are available only at 60 and 100  $\mu\text{m}$ . Four galaxies in the sample have been observed with the C200 array camera with one filter only; in order to estimate their dust temperature we acquired photometric points at 60 and 100  $\mu\text{m}$  using IRAS sky-survey data, processed with SCANPI.

Although the ISO data offer a great improvement compared to previous dust temperature determinations in early-type galaxies, which were based on IRAS data only, the SEDs are not sufficiently sampled to allow us to establish strong and definitive interpretation of the FIR dust emission if  $\beta$  is allowed to be a completely free parameter. There are no sub-millimeter data available for the galaxies in our sample. Fortunately, theoretical absorption efficiencies for typical silicate or carbon grains suggest  $\beta \approx 2$  and  $\beta > 1$  at very long wavelengths because of the Kramers-Kronig relations. With this in mind we explore two possible models for fitting the SEDs: a single-temperature blackbody model modified with variable  $\beta$ , and a two-temperature modified blackbody model with fixed  $\beta = 2$ .

7.2.1. *Single modified blackbody*

The modified blackbody emission from dust at a single temperature is

$$F_\nu = A\nu^\beta B_\nu(T_D) \tag{1}$$

While the amplitude  $A$ , the dust temperature  $T_D$ , and  $\beta$ , are all free parameters, values of the exponent  $\beta$  are constrained to the range  $1 \leq \beta \leq 2$ , guided by representative values of the dust emissivity in the Milky Way and other well-observed external galaxies. Fits to equation (1) are performed by minimising the  $\chi^2$  and evaluated using the reduced  $\chi^2$  to account for the number of data points that sample the SED in each galaxy. The index  $\beta$  affects the slope in the Rayleigh-Jeans region: small values produce a flatter slope and large values tend to make it steeper. Since the wavelength coverage in our sample is limited to  $\lambda \leq 200 \mu\text{m}$ , the Rayleigh-Jeans tail is not fully sampled, making the  $\beta$  fitting procedure uncertain. For example, Klaas et al. (2001) found significant discrepancies in  $\beta$  between fits to the full galactic FIR spectrum as opposed to using only the FIR data points.

Aware of this limitation, our first single-temperature fits to the SEDs regard  $\beta$  as a free parameter. The fitted parameters are shown in Table 9 together with the reduced  $\chi^2$ . Most of the  $\beta$  values are very small, approaching the lower allowed limit of 1. If  $\beta$  is unrestricted, the best fit would provide unrealistic values well below 1 for the majority of the galaxies. This is clearly due to the lack of sufficient data points in the sub-millimeter region, and is a manifestation of an unreliable fit rather than an indication of unusually low  $\beta$ . Only 8 of the 28 galaxies detected have acceptable fits under the  $\chi^2$  criterion. The large majority of the galaxies could not be fitted with a single-temperature model. The mean value for the dust temperature  $T_D$  derived by the fit is 27.9 K, spanning a range from 22 to 43 K.

It is difficult to reconcile specific estimates of  $\beta$  with a unique dust composition, size distribution and temperature (see Dunne & Eales, 2001, for a short review on  $\beta$  values in the literature). Almost all observations of external galaxies report values of  $\beta$  between 1.6 and 2, with  $\beta=2$  be the most accredited (e.g. Chini et al. 1989, Chini & Krugel 1993, Bianchi et al. 1998). However, FIR emission from grains with small  $\beta$  may contribute less to the SED when averaged over the entire galaxy. Nevertheless, following previous observations, we also performed single modified blackbody fits with fixed  $\beta=2$ . These temperatures are reported in Table 9 along with the reduced  $\chi^2$ . With  $\beta$  fixed at 2, only four galaxies are compatible with a single-temperature model and the other 24 require at least two dust components. The temperatures have a mean of 23.8 K with a range of 19 - 34 K. With this steeper  $\beta=2$  emissivity, the average temperature is colder by  $\sim 4$  K, confirming a trend already reported in the literature (Bendo et al. 2003).

Errors in the dust temperature arise from uncertainties in the ISOPHOT photometry and the assumed grain emissivity. Since our ISOPHOT data are calibrated to the COBE-DIRBE flux scale, we are confident that calibration errors are lower than the generally assumed 30 percent except

for the faintest objects with very low signal-to-noise ratios. We estimated the error in the derived temperatures by varying the fluxes at the shortest and longest wavelength: we increased the 60  $\mu\text{m}$  flux by 20% and decreased the 200  $\mu\text{m}$  flux by 20% and vice-versa. The estimated errors are of the order  $\sim 2$  K for the entire sample.

### 7.2.2. Two modified blackbodies

In the previous section we showed that the SEDs for most of the sources could not be fitted with a single-temperature model if  $\beta = 2$ . We now consider spectral models in which the SED is fit with two dust components (warm and cold), each having modified blackbody spectra given by equation (1), and assuming a fixed  $\beta=2$  dust emissivity index. Four free parameters describe the temperatures and amplitudes of the two modified blackbodies and these parameters were used to construct  $\chi^2$  fits to the data. Six galaxies detected using the PHT 37/39 mode have been observed in three ISOPHOT bands only, for which the two-component fits are under-constrained. For these galaxies we assume that the warm dust temperature is 43 K, the mean warm dust temperature derived for galaxies observed at four or more wavelengths. We note that the temperature of the cold dust is insensitive to relatively large variations of the assumed warm dust temperature for these galaxies. The fitted warm and cold dust temperatures are listed in Table 9. The cold dust component temperatures range from 17 to 24 K with an average of 19.5 K. In all likelihood, the dust temperatures are not confined to two temperatures, but span a continuum between them. Finally, our dust temperatures compare well with the temperature  $\sim 18$  K found by Stickel et al. (2003) for M86. Using the same method described in the previous section, the estimated errors on the derived temperatures due to uncertainties in the flux densities are  $\leq 10\%$  for both warm and cold components. Neither the warm nor cold dust temperatures correlate with  $L_B$ .

It is interesting to compare the derived temperatures of the four galaxies, NGC 1395, NGC 1553, NGC 4261, NGC 4552, for which the SEDs are consistent with both fitting models. For all but one (NGC 4552) the one-temperature fit is warmer by less than 2 K relative to the cold temperature fit in the two-blackbody model. This is within the estimated error in the derived temperature due to uncertainties in the fluxes. For NGC 4552, the discrepancy in temperature between the two fitting model is  $\sim 5$  K.

We also estimated the dust temperature using only the 60 and 100  $\mu\text{m}$  ISO flux densities, the same wavelengths available to IRAS. A single component dust temperature fit to the ISOPHOT 60 and 100  $\mu\text{m}$  flux densities yields a mean dust temperature for all detected galaxies of 29.1 K, which is significantly larger than the mean cold dust temperature 19.5 K found using all the ISO photometric data.

### 7.3. Dust Masses

The dust masses can be estimated using the parameters that fit the dust SED and the standard relation (Hildebrand 1983; Draine 1990):

$$M_d = \frac{F_\lambda D^2}{k_\lambda B_\lambda(T_D)} \quad (2)$$

where  $F_\lambda$  is the observed flux density at wavelength  $\lambda$ ,  $D$  is the galaxy distance, and  $k_\lambda$  is the dust opacity.

The derived dust masses depend critically on the dust temperatures, the dust emissivity index  $\beta$ , and the opacity  $k_\lambda$ . Dust masses are notoriously uncertain (e.g. Devereux & Young 1990). We adopted the opacities calculated by Li & Draine (2001),  $81 \text{ cm}^2 \text{ g}^{-1}$  and  $9 \text{ cm}^2 \text{ g}^{-1}$  at  $60 \mu\text{m}$  and  $180 \mu\text{m}$ , respectively, which are representative of currently considered values. The masses were derived from the flux values at  $180 \mu\text{m}$ ; for the two-blackbody model the “warm” dust component was estimated using fluxes at  $60 \mu\text{m}$ . The value of  $k_\lambda$  was adjusted to be consistent with the value of  $\beta$  assumed for the FIR emission. Table 9 lists the dust masses calculated for each of the three models used in fitting the SEDs. Higher temperatures derived in the single-blackbody fits correspond to lower calculated dust masses. Also, dust masses are higher when calculated with larger values of  $\beta$ . The reason for this is twofold: (i) larger  $\beta$  results in lower dust temperatures that decrease the value of  $B_\lambda(T_D)$  in the denominator of equation (2), and (ii)  $k_\lambda$  at  $180 \mu\text{m}$  is lower when larger  $\beta$  values are used.

Clearly, the FIR emission from dust at a single temperature cannot fit the spectra of most of our early type galaxies. However, a combination of a warm and cold dust components provides an acceptable representation of the observed FIR. Although the two-temperature fits must be taken with some caution, we consider the dust masses derived in this way the best estimate of the dust content in these galaxies.

The mass of dust in the cold component is about 3 orders of magnitude larger than the mass of warm dust. The dust content is not small. Several galaxies have dust masses near  $10^7 M_\odot$ . As pointed out by Dale & Helou (2002), the dust masses may be underestimated by a factor of few when the SEDs are fitted with one or two blackbodies instead of considering a (more realistic) continuous range of blackbodies corresponding to a range of dust heating environments.

The total dust mass does not correlate with  $L_B$  over the limited range of  $L_B$  represented in the sample. This again may indicate a stochastic external origin for the dust. Table 9 also shows upper limits to the dust mass evaluated for galaxies that were not detected with ISO. These upper limits have been constructed using the  $3\sigma$  fluxes and assuming a mean dust temperature of 19.5 K. This is not strictly a true upper limit to the dust mass since the actual temperature may be lower than the assumed one, but it provides a useful estimate.

It is important to stress that photometry at wavelengths greater than  $100 \mu\text{m}$  are necessary to

view the dust SED around its peak emission and are therefore critical in determining the total dust mass. Estimates of dust temperatures based on the flux ratio  $F_{60}/F_{100}$  can severely underestimate the derived dust mass. In Figure 8 we compare our estimated dust masses with values derived from IRAS temperatures (Roberts et al. 1991; Goudfrooij et al. 1994; Bregman et al. 1998) scaled to our assumed distances. The lower dust temperature indicated by ISO increases the estimated dust mass by factors of  $\langle M_{d,ISO}/M_{d,IRAS} \rangle \sim 12$ , 24, and 16 when compared to the IRAS masses given by Roberts et al. (1991), Goudfrooij et al. (1994), and Bregman et al. (1998), respectively.

#### 7.4. Angular extent of the dust emission

The spatial distribution of the dust in elliptical galaxies is poorly known. Most early-type galaxies show dust absorption features in the very center (e.g. van Dokkum & Franx 1995), but very little is known about the presence of an extended component of dust. It is well known that for elliptical galaxies the dust mass estimated from FIR fluxes is much larger than the dust mass derived from optical absorption studies (Goudfrooij & de Jong 1995). This discrepancy may be solved if most of the dust is smoothly distributed in a large volume.

ISO observations in the PHT 32 AOT mode may shed light on the extension of the FIR emission. Many of the galaxies observed in the oversampled map mode have been selected because their  $D_{25}$  diameters are much larger than the ISO telescope beam. For example, with a sky sampling of  $15'' \times 23''$  at 60, 90 and 100  $\mu\text{m}$  the PHT 32 AOTs approach the Nyquist limit, which is  $\sim 17''$  for the ISO telescope at 100  $\mu\text{m}$ . These observations have the potential to resolve the galaxies and to determine if the far-infrared emission is produced by dust distributed throughout the galaxy or by the central dust clouds found in optical surveys. In principle, the spatial distribution of the FIR emission may also reveal information about the controversial origin of the dust in the elliptical galaxies. Dust accreted in a recent merger is expected to have an extended, asymmetric distribution, while internally produced dust should have a more compact and regular aspect. However, the faint level of the FIR emission in early-type galaxies and the relatively poor spatial resolution of ISOPHOT do not allow a secure study of the asymmetries in the dust distribution.

To identify galaxies in the PHT 32 AOT sample that are more extended than the PSF at FIR frequencies, we developed an image modeling procedure to apply to the oversampled map data. We performed a beam-fit for sources that appear point-like and modeled sources with a two-dimensional gaussian image if there is evidence for some detected extension. Since there is no analytical description of the shape of a true beam, we first constructed a beam-model based on a circular gaussian. Using the PIA Map Simulator, we constructed noiseless maps of a point source by setting the sampling parameters in the same way they were set in acquiring the actual PHT 32 data. After correcting the simulated maps for transients, the derived widths of the gaussian beam-fit model correspond to  $\sigma=18''.60$ ,  $20''.25$ ,  $20''.40$ ,  $39''.90$ ,  $40''.80$ , and  $41''.10$  at 60, 90, 100, 150, 180, and 200  $\mu\text{m}$ , respectively, where the  $\text{FWHM} = 2.354\sigma$ . We used these model beams to fit pointlike sources.

The observed emission from extended sources was found by convolving the circular beam-fit model with an elliptical gaussian source model. The parameters that must be adjusted to achieve a fit to an extended source are the amplitudes, rotation angles, and sigmas of the two gaussians along the principal axes of the elliptical source model. We used an optimization routine from the IDL Library to minimize a multi-parameter function, determining the parameters for the best fit. The PHT 32 maps are undersampled in the cross-scan ( $z$ ) direction. Therefore, before performing each model fit, we re-sampled the data in the  $z$  direction using a gridding algorithm in PIA.

This simple image fitting procedure is well suited to match the surface brightness profiles of elliptical galaxies where the galaxy morphology is rather smooth and regular. Two galaxies in the sample - NGC 2293 and NGC 4649 - are either in close interaction with companions or have a complex brightness profile. As a consequence our elliptical model is not appropriate to describe the light profiles for these two galaxies so we have not attempted to model them.

Among the 10 galaxies that have been detected with PHT 32, four appear to be resolved by ISOPHOT at least in some of the bands observed. In some cases the angular extent derived by the model-fit is only marginally larger than the instrumental beam, making our estimate rather uncertain. Table 10 shows the angular extent of the infrared emission of the source ( $\sigma_{S,major}$ ,  $\sigma_{S,minor}$ ) at the various wavelengths and other parameters of the model fits for these galaxies with extended FIR images. The gaussian scales  $\sigma_S$  and  $\sigma_T$  refer to the source model and the the convolution of the source model with the beam model, respectively, so  $\sigma_S \leq \sigma_T$  is always expected.

At 200  $\mu\text{m}$  NGC 5666 shows a complex and extended surface brightness structure for which a multi-component model would be more appropriate than our elliptical gaussian model. Consequently, the angular size for NGC 5666 in Table 10 based on our gaussian model should be regarded as approximate. NGC 4261 and NGC 5173 have been clearly detected at the wavelengths shown in Table 10, but they are faint and their low S/N ratios make the determination of the ellipsoid position angle quite uncertain. The extension of the ISO image for NGC 4261 exceeds both the size of the central dusty disk  $\sim 2''$  seen in HST images (Jaffe et al. 1993) and the dust feature  $15''$  distant from the galactic center (Moellenhoff & Bender 1987). For each of the three galaxies in Table 10 that have been observed at more than one ISO band, the size of the source  $\sigma_S$  increases steadily with increasing wavelength and often exceeds the optical half light radius  $R_e$ . Such a behavior would be expected if the dust is heated by stellar radiation which decreases from the galactic center

Figure 9 shows the observed brightness profiles (histogram) together with their model fits (solid line). The beam-fit profiles for point sources are shown with dashed lines. To illustrate the likelihood or degree of spatial extension, we show both the model-fit and beam-fit for many galaxies. For each FIR band the middle panels in Figure 9 show fits to the row positioned on the galaxy center along the scan direction ( $y$ -axis). The top and bottom panels show off-source parallel scans taken at two symmetric positions on both sides of the source. The offset in the  $z$  direction (the cross-scan direction) is noted in each plot.

We also compared the effective radius  $R_e$  of the galaxies that were not resolved with PHT 32 with the ISOPHOT beam sizes. Among the 6 detected galaxies that appear as pointlike, two (NGC 3998 and NGC 5813) have effective radius  $\sim 2$  times larger than the  $\sigma \sim 20''$  of the beam at 60 and 100  $\mu\text{m}$ . At least for these two galaxies, this is indicative that most of the FIR is coming from the central dust cloud known to exist in both galaxies. At larger wavelengths, the effective radius become comparable to the size  $\sigma$  of the beam.

## 8. Conclusions

We extracted FIR data for a sample of early-type galaxies from the ISO archives. The data extracted are described in Table 1 and the sample is described in Table 2. It includes 53 giant galaxies: 39 ellipticals and 14 S0 (or later) galaxies, as classified in the RSA catalog. The data reduction and calibration give very consistent results, both for point sources and extended objects. We tested and verified the photometric performance of ISO by comparing with data obtained previously. A comparison with IRAS observations of the same early-type galaxies serves as an independent calibration check for the ISO response to faint discrete sources. The integrated fluxes found with ISO match IRAS fluxes within a few percent for point sources. Moreover, the sky brightness is in good agreement with COBE-DIRBE results. Based on these comparisons, we are confident that a reliable ISO calibration has been established.

The most important contribution provided by ISO are the data at longer wavelengths ( $\lambda > 100 \mu\text{m}$ ). This allows a much more accurate determination of the dust temperature and dust mass than was possible with previous IRAS data. We find that the FIR spectral energy distribution requires emission from dust with at least two different temperatures. The mean temperature of the hot dust component is 43 K, while the cold dust, which is always the dominant component by mass, has a mean temperature of 20 K. By contrast, the dust temperature derived by fitting the IRAS data results in a single temperature that is about 10 K higher. We suspect that our two-temperature dust models represent the extremes of a continuum of dust temperatures.

Typically, the dust mass ranges from  $10^5$  to more than  $10^7 M_\odot$ . The dust masses derived from ISO data are on average at least ten times greater than those previously estimated from IRAS observations (Roberts et al. 1991). Using the Galactic dust to gas mass ratio,  $\sim 0.01$ , the total mass of cold gas associated with this dust could be in the range  $10^7$  to more than  $10^9 M_\odot$ .

The lack of any recognizable correlation between  $L_{FIR}$  or dust mass and  $L_B$  suggests that the dust in at least some of our sample galaxies has been acquired externally in a merger event. While the ISO data provide new and useful information about FIR emission from early-type galaxies, the sample of archival data is far from ideal. It is likely that many galaxies selected for ISO observations were chosen because they were known to have large IRAS fluxes or large masses of cold gas. Elliptical galaxies with cold HI or molecular gas are rare and probably unrepresentative. Such galaxies are likely to have experienced unusual dust-rich mergers that could mask physically



interesting correlations expected from internally produced dust. But it is unclear if mergers are the dominant source of dust in E and S0 galaxies. For example, if most of the FIR is emitted by central dust clouds, these clouds could be disturbed at irregular intervals by low level AGN activity in the galactic cores, creating the stochastic  $L_{FIR}$  variation in our sample. Furthermore, the sensitivity of IRAS and ISO are not sufficient to detect FIR emission from many optically luminous E galaxies such as NGC 4472. While there is clear evidence of circumstellar mid-IR emission from mass-losing red giants, the FIR emission studied so far cannot be unambiguously attributed to the same dust when it becomes truly interstellar. To make progress, it will be necessary to obtain deeper FIR observations from a more representative, optically-selected sample.

The data presented in this paper were taken in guaranteed observing time made available by the following PIs: Bregman, J. N., Knapp, G., Macchetto, F., Norgaard-Nielsen, H. U., Renzini, A. and Vigroux, L.; we thank the referee for a careful reading of the manuscript, and for a number of comments and suggestions that helped to make it clearer. This study is supported by NASA grant NRA-01-01-ADP-032 for which we are very grateful. FB is supported in part by grants MURST-Cofin 00 and ASI-ARS99-74. WGM is supported by NASA grants NAG 5-8409 & NAG 5-13275 and NSF grants AST-9802994 & AST-0098351. Finally, this research has made use of the NASA/IPAC Infrared Science Archive, which is operated by the Jet Propulsion Laboratory, California Institute of Technology, under contract with the National Aeronautics and Space Administration.

## APPENDIX

Following the procedure described in detail by Tuffs et al. (2002), we developed a scheme to analyze our PHT 32 data to detect and quantify the spatial extent of the FIR emission. First we determine an appropriate circular gaussian beam-fit for pointlike sources and then we compare this to an ellipsoidal beam-model for the source. Extended sources are assumed to have gaussian profiles along each axis of the ellipsoid. An optimization routine from the IDL library is used to minimize a multi-parameter function and to determine the amplitudes, position angle and ellipticity for the best-fit. We first constructed a beam-model based on a circular gaussian as described in § 7.4. To account for the difference in shape between the true beam profile and the gaussian model, a correction factor must be applied to the flux density derived by integrating the beam model. We evaluated these corrections by generating a simulated map of a point source of known flux density using the PIA Map Simulator. From the simulated maps corrected for transients, we found that the derived flux densities were less than the original value entered in the simulation maps at all wavelengths. The correction factors range from 0.84 at 90  $\mu\text{m}$  to 0.89 at 200  $\mu\text{m}$ . We applied these corrections to the computed flux densities for all beam-fits performed on pointlike sources. The fit for the extended sources was performed by convolving a beam-fit model with an elliptical gaussian source model; the amplitudes, rotation angles and sigmas of the gaussian source model were adjustable parameters in the fit.

## REFERENCES

- Athey, A., Bregman, J. N., Bregman, J. D., Temi, P. & Sauvage, M. 2002, *ApJ*, 571, 272
- Bendo, G. J., Joseph, R. D., Wells, M., Gallais, P., Haas, M., et al. 2003, *AJ*, 125, 2361
- Bianchi, S., Alton, P. B., Davies, J. I., Trewhella, M., 1998, *MNRAS*, 298, L49
- Braine, J., Henkel, C., Wiklind, T., 1997, *A&A*, 321, 765
- Bregman, J. N., Snider, B. A., Grego, L., Cox, C. V., 1998, *ApJ*, 499, 670
- Brown, B. A. & Bregman, J. N., 1998, *ApJ*, 495, L75
- Caon, N., Macchetto, D., Pastoriza, M. 2000, *ApJS*, 127, 39
- Chini, R., Krugel, E., Kreysa, E., Gemuend, H. P., 1989, *A&A*, 216, L5
- Chini, R. & Krugel, E., 1993, *A&A*, 279, 385
- Dale, D. A. & Helou, G., 2002, *ApJ*, 576, 159
- Devereux, N. A. & Young, J. S., 1990, *ApJ*, 359, 42
- Draine, B. T., 1990, *The Interstellar Medium in Galaxies*, eds. H.A. Thronson Jr., J. M. Schull, p.483
- Dunne, L. & Eales, S. A., 2001, *MNRAS*, 327, 697
- Eskridge, Paul B., Fabbiano, Giuseppina, Kim, Dong-Woo, 1995, *ApJ*, 448, 70
- Faber, S. M., Wegner, G., Burstein, D., Davies, R., et al. 1989, *AJ*, 69, 763
- Faber, S. M., Tremaine, S., Ajhar, E. A., Byun, Y., et al. 1997, *AJ*, 114, 1771
- Ferrari, F., Pastoriza, M. G., Macchetto, F. D., Caon, N., 1999, *A&AS*, 136, 269
- Ferrari, F., Pastoriza, M. G., Macchetto, F. D., Bonatto, C., Panagia, N., and Sparks, W. B. 2002, *A&A*, 389, 355
- Forbes, D. A., 1991, *MNRAS*, 249, 779
- Gabriel, C., Acosta-Pulido, J., Heinrichsen, I., Morriss, H., & Tai, W-M., *A.S.P. Conference Series*, Vol. 125, 1997, p. 108.
- Goudfrooij, P., 1994, *PhD Thesis* University of Amsterdam.
- Goudfrooij, P., Hansen, L., Jorgensen, H. E., Norgaard-Nielsen, H. U., 1994, *A&AS*, 105, 341
- Goudfrooij, P. & de Jong, T., 1995, *A&A*, 298, 784

- Hildebrand R. H., 1983, QJRAS 24, 267
- Huchtmeier, W. K., 1994, A&A, 286, 389
- Huchtmeier, W. K., Sage, L. J., Henkel, C., 1995, A&A, 300, 675
- Jaffe, W., Ford, H. C., Ferrarese, L., van den Bosch, F., O’Connell, R. W., 1993, Nature, 364, 213
- Jura, M., Kim, D. W., Knapp, G. R., Guhathakurta, P., 1987, ApJ, 312, L12
- Kelsall, T., Weiland, J. L., Franz, B.A., et al., 1998, ApJ, 508, 44
- Kessler M. F., Steinz U. A., Anderegg M. E., et al., 1996, A&A, 315, L27
- Klaas, U., Laureijs, R. J., Radovich, M. and Schulz, B. 1998, ISOPHOT Calibration Accuracies, SAI/98-092/rp
- Klaas, U., Wilke, K., Kiss, C., Radovich, M. and Richards, P., 2000 SAI/2000-014/Rp, Version 2.0
- Klaas, U., Haas, M., Muller, S. A. H., Chini, R., Schulz, B., et al. 2001, A&A, 379, 823
- Laureijs, R. J., Klaas, U., Richards, P. J., Schulz, B., and brahm, P., 2002, The ISO Handbook Volume IV: PHT - The Imaging Photo-Polarimeter, Version 2.0, SAI-99-069, ESA
- Knapp, G. R. & Raimond, E., 1984, A&A, 138, 77
- Knapp, G. R., Guhathakurta, P., Kim, D-W., Jura, M. A. 1989, ApJS, 70, 329
- Knapp, G. R., Gunn, J. E., Wynn-Williams, C. G., 1992, ApJ, 399, 76
- Knapp, G. R., Rupen, M. P., Fich, M., Harper, D. A., Wynn-Williams, C. G., 1996, A&A, 315, L76
- Lake, G., Schommer, R. A., van Gorkom, J. H., 1987, ApJ, 314, 57
- Laureijs, R. J., Klaas, U., Richards, P. J. and Schulz, B. 1998, ISOPHOT Data User Manual, SAI/95-220/Dc
- Laureijs, R. J. & Klaas, U. 1999, ISOPHOT Error Budgets, SAI/99-091/Dc
- Laureijs, R. J. 1999, IDC PHT Internal Calibration Report, Version 1.0, 1999
- Lees, J. F., Knapp, G. R., Rupen, M. P., Phillips, T. G., 1991, ApJ, 379, 177
- Lemke D., Klaas U., Abolins J., et al., 1996, A&A, 315, L64
- Li, Aigen & Draine, B. T., 2001, ApJ, 554, 778
- Malhotra, S., Hollenbach, D., Helou, G., Silbermann, N. Valjavec, E., 2000, ApJ, 543, 634

- Mathews, W. G. & Brighenti, F., 2003, *ApJ*, 590, L5
- Moellenhoff, C. & Bender, R., *A&A*, 174, 63
- O’Sullivan, E, Forbes, D. A., Ponman, T. J., 2001, *MNRAS*, 328,461
- Ott, S, Abergel, A., Altieri, B., Augeres, J. L., Aussel, H., et al. 1997, *ASP Conf. Ser. Vol. 125, Astronomical Data Analysis Software and Systems (ADASS) VI*,ed. G. Hunt & H.E.Payne, 34
- Paturel, G., Andernach, H., Bottinelli, L., di Nella, H., et al., 1997, *A&AS*, 124, 109
- Popescu, C. C., Tuffs, R. J., Volk, H. J., Heinrich, J., Pierini, D., Madore, D. F. 2002, *ApJ*, 567, 221
- Ravindranath, S., Ho, L. C., Peng, C. Y., Filippenko, A. V., & Sargent, W. L. W. 2001, *ApJ* 122, 653
- Reach, W. T., 2000, *SIRTF Background Estimation: Method and implementation.*
- Richards, P. & Klaas, U., 2002, Report on the Scientific validation of the mini-map photometry processing in the PHT pipeline.
- Roberts, M. S., Hogg, D. E., Bregman, J. N., Forman, W. R., Jones, C., 1991, *ApJS*, 75, 751
- Sadler, E. M., Oosterloo, T. A., Morganti, R., Karakas, A., 2000, *AJ*, 119, 1180
- Sofue, Y. & Wakamatsu, K., 1993, *PASJ*, 45, 529
- Sandage, A. & Tamman, G. A., 1981, *Carnegie Inst. of Washington, Publ.* 635
- Sandage, A. & Bedke, J., 1994, *The Carnegie Atlas of Galaxies, Vol.1*
- Sarazin, C. L., Irwin, J. A. Bregman, J. N., 2001, *ApJ*, 556, 533
- Schlegel, D., Finkbeiner, D., Davis, M. 1998, *ApJ*500, 525
- Stickel, M., Bregman, J. N., Fabian, A. C., White, D. A., Elmegreen, D. M. 2003, *A&A*, 397, 503
- Taniguchi, Y. & Watanabe, M., 1987, *ApJ*, 313, 89
- Temi, P., Mathews, W. G., Brighenti, F., Bregman, J. D., 2003, *ApJ*, 585, L121
- Trinchieri, G. & Goudfrooij, P., 2002, *A&A*, 386, 472
- Tsai, J. C. & Mathews, W. G. 1995, *ApJ*, 448, 84
- Tsai, J. C. & Mathews, W. G. 1996, *ApJ*, 468, 541
- Tuffs, R. J., Popescu, C. C., Pierini, D., Volk, H. J., 2002, *ApJS*, 139, 37

Tuffs, R. J., & Gabriel, C., 2002, In Press.

van Dokkum, P. G. & Franx, M., 1995, AJ, 110, 2027

Wiklind, T., Combes, F., Henkel, C., 1995, A&A, 297, 643

Fig. 1.— Layout of the PHT 22 mini-maps. The top panel shows the C100 layout for a  $3 \times 3$  raster map. Each square represent a pixel of  $46''$  in size, and a black filled dot marks each position in the raster grid. The grayscale intensity changes as a function of the number of observations in that specific position. The central position has been observed 9 times during the scan, while the four corners have only one measurement. The thick dashed square represent the  $3 \times 3$  C100 detector array. The bottom panel gives the  $4 \times 2$  raster layout for the C200  $2 \times 2$  pixel array; each pixel is  $92''$  in size. The central map position has been observed 4 times. For both arrays the raster step is equal to the size of one pixel.

Fig. 2.— ISOPHOT backgrounds at several far-infrared filters against brightness derived from a model based on COBE-DIRBE data. Data for the background model were color-corrected and evaluated toward the position of each galaxy and at the same epoch when the ISO observations were recorded. Each panel shows measurements at all the available ISOPHOT bands for a specific observing mode. Panels (a) through (d) present data for the PHT 32, PHT 37/39, PHT 22 mini-maps, and PHT 22 single-pointing, respectively. Each symbol identifies a wavelength band: (\*) is  $60\mu\text{m}$  band, (+) is  $90\mu\text{m}$  band, ( $\diamond$ ) is  $100\mu\text{m}$  band, ( $\triangle$ ) is  $150\mu\text{m}$  band, ( $\square$ ) is  $180\mu\text{m}$  band, and ( $\times$ ) is  $200\mu\text{m}$  band.

Fig. 3.— Integrated flux density of a sample of early-type galaxies observed with ISO C60 (left panel) and C100 (right panel) filters versus the flux density measured by IRAS in the  $60$  and  $100\mu\text{m}$  bands. The color-corrected ISO fluxes, have been recorded using the PHT 32, PHT22, and PHT37/39 observing modes. The straight line represents the one-to-one correlation between the ISO and IRAS integrated fluxes.

Fig. 4.— ISO FIR luminosities in the various bands vs.  $L_B$ . In panel (b) we have grouped together galaxies detected at  $90\mu\text{m}$  with those detected at  $100\mu\text{m}$ . Panel (c) includes data at  $150$ ,  $170$  and  $180\mu\text{m}$ . Filled circles indicate elliptical galaxies, open circles indicate S0 or later galaxies. The four dwarf ellipticals and NGC 1275 are not shown in this plot.

Fig. 5.—  $L_{15\mu\text{m}}/L_B$  vs.  $L_{FIR}/L_B$ . As in Figure 4 panel (b) include data at  $90$  and  $100\mu\text{m}$ , while panel (c) include data at  $150$ ,  $170$  and  $180\mu\text{m}$ . Filled circles denote ellipticals, open circles S0 or later galaxies.

Fig. 6.— ISO FIR luminosities vs.  $L_x$ . Panel (b) include data at  $90$  and  $100\mu\text{m}$ , panel (c) include data at  $150$ ,  $170$  and  $180\mu\text{m}$ . Filled symbols denote ellipticals, open symbols S0 or later galaxies. Left-pointing triangles indicate upper limits in  $L_x$ .

Fig. 7.— FIR Spectral Energy Distribution of the detected galaxies in the sample. Color-corrected flux densities are plotted with their associated error bars. The dotted lines show the two modified blackbody functions that best fits the data. The sum of the "warm" and "cold" fitting functions are represented by the solid line. The fitting temperatures for the cold dust component are marked in the upper right corner. For the galaxies with only three photometric points, a warm dust temperature  $T=43$  has been assumed.

Fig. 8.— ISO Dust masses vs. IRAS dust masses. Filled circles refer to IRAS data from Roberts et al. 1991; open squares are from Goudfrooij et al 1994; open circles are from Bregman et al 1998. IRAS masses have been scaled to our assumed distances. The solid line represents the 1:1 relation.

Fig. 9.— Three surface brightness profiles are shown for each observed galaxy. The central panel shows the variation along the scan direction (y-axis) passing through the center of the source. The upper and lower panels show similar nearby parallel scans displaced symmetrically from the source in a perpendicular direction (z-axis) by the amount shown. The beam-fits corresponding to pointlike sources are plotted as dashed lines. The solid lines show beam-models that are broader than the pointlike response for those relatively few sources that are extended.

Table 1. Logs of the Observations

Name	$\alpha(2000)$	$\delta(2000)$	TDT <sup>a</sup>	AOT <sup>b</sup>	Filter	$N \times M^c$	f.o.v. "×"	$T_{int}^d$ (s)
NGC 0147 .....	00 33 12.12	+48 30 20.5	80104478	PHT22	C60	3 × 3	227x227	420
	00 33 12.12	+48 30 20.5	80104478	PHT22	C90	3 × 3	227x227	420
	00 33 12.12	+48 30 20.5	80104479	PHT22	C160	4 × 2	457x273	19
	00 33 12.12	+48 30 20.5	80104479	PHT22	C200	4 × 2	457x273	195
NGC 0185 .....	00 38 56.90	+48 20 10.9	78500680	PHT22	C60	3 × 3	227x227	420
	00 38 56.90	+48 20 10.9	78500680	PHT22	C90	3 × 3	227x227	420
	00 38 56.90	+48 20 10.9	78500681	PHT22	C160	4 × 2	457x273	195
	00 38 56.90	+48 20 10.9	78500681	PHT22	C200	4 × 2	457x273	195
	00 38 57.60	+48 20 11.9	40001320	CAM01	LW3	...	210x210	2200
NGC 0221 .....	00 42 43.06	+40 51 56.4	80800683	PHT22	C60	3 × 3	227x227	420
	00 42 43.06	+40 51 56.4	80800683	PHT22	C90	3 × 3	227x227	420
	00 42 43.06	+40 51 56.4	80800684	PHT22	C160	4 × 2	457x273	195
	00 42 43.06	+40 51 56.4	80800684	PHT22	C200	4 × 2	457x273	195
NGC 0596 .....	01 32 52.45	-07 01 54.8	80200585	PHT22	C60	3 × 3	227x227	420
	01 32 52.45	-07 01 54.8	80200585	PHT22	C90	3 × 3	227x227	420
	01 32 52.45	-07 01 54.8	80200586	PHT22	C160	4 × 2	457x273	195
	01 32 52.45	-07 01 54.8	80200586	PHT22	C200	4 × 2	457x273	195
NGC 0720 .....	01 53 00.00	-13 44 20.8	80200687	PHT22	C60	3 × 3	227x227	420
	01 53 00.00	-13 44 20.8	80200687	PHT22	C90	3 × 3	227x227	420
	01 53 00.00	-13 44 20.8	80200688	PHT22	C160	4 × 2	457x273	195
	01 53 00.00	-13 44 20.8	80200688	PHT22	C200	4 × 2	457x273	195
NGC 0807 .....	02 04 55.72	+28 59 20.2	43603048	PHT32	C135	4 × 2	457x273	352
NGC 0821 .....	02 08 21.48	+10 59 42.1	81200689	PHT22	C60	3 × 3	227x227	420
	02 08 21.48	+10 59 42.1	81200689	PHT22	C90	3 × 3	227x227	420
	02 08 21.48	+10 59 42.1	81200690	PHT22	C160	4 × 2	457x273	195
	02 08 21.48	+10 59 42.1	81200690	PHT22	C200	4 × 2	457x273	195
NGC 1172 .....	03 01 35.91	-14 50 11.9	79601303	PHT32	C135	5 × 5	549x549	1209
	03 01 35.91	-14 50 11.9	79601404	PHT32	C180	5 × 5	549x549	1207
NGC 1275 .....	03 19 48.61	+41 30 38.1	84002593	PHT22	C160	4 × 4	457x457	395
	03 19 48.61	+41 30 38.1	84002593	PHT22	C200	4 × 4	457x457	395
	03 19 48.16	+41 30 42.7	61503617	CAM01	LW3	...	210x210	382
NGC 1332 .....	03 26 17.27	-21 20 09.2	59301002	PHT37/39	C60	...	135x135	266
	03 26 17.27	-21 20 09.2	59301002	PHT37/39	C100	...	135x135	266
	03 26 17.27	-21 20 09.2	59301004	PHT37/39	C180	...	181x181	212
	03 26 17.24	-21 20 09.4	59301005	CAM01	LW10	...	204x204	526
NGC 1344 .....	03 28 18.98	-31 04 04.0	78100608	PHT32	C60	4 × 4	411x342	1428
	03 28 18.98	-31 04 04.0	78100608	PHT32	C90	4 × 4	411x342	1428
	03 28 18.98	-31 04 04.0	78100709	PHT32	C180	4 × 3	457x365	482



Table 1—Continued

Name	$\alpha(2000)$	$\delta(2000)$	TDT <sup>a</sup>	AOT <sup>b</sup>	Filter	$N \times M^c$	f.o.v. "×"	$T_{int}^d$ (s)
NGC 1395 .....	03 38 29.54	-23 01 39.8	84801096	PHT22	C60	3 × 3	227x227	420
	03 38 29.54	-23 01 39.8	84801096	PHT22	C90	3 × 3	227x227	420
	03 38 29.54	-23 01 39.8	84801097	PHT22	C160	4 × 2	457x273	195
	03 38 29.54	-23 01 39.8	84801097	PHT22	C200	4 × 2	457x273	195
	03 38 29.57	-23 01 39.9	84800902	CAM01	LW10	...	198x198	180
NGC 1553 .....	04 16 10.27	-55 46 51.2	68900708	PHT37/39	C60	...	135x135	362
	04 16 10.27	-55 46 51.2	68900708	PHT37/39	C100	...	135x135	362
	04 16 10.27	-55 46 51.2	68900710	PHT37/39	C180	...	181x181	468
	04 16 10.29	-55 46 51.2	68900711	CAM01	LW10	...	204x204	536
NGC 2293 .....	06 47 42.79	-26 45 10.8	71102227	PHT32	C60	5 × 5	503x411	1027
	06 47 42.79	-26 45 10.8	73901028	PHT32	C100	5 × 5	503x411	873
	06 47 42.79	-26 45 10.8	72401330	PHT32	C200	5 × 5	549x549	805
NGC 2328 .....	07 02 36.31	+42 04 06.0	73102932	PHT32	C135	4 × 2	457x273	352
	07 02 36.31	+42 04 06.1	71002838	CAM01	LW3	...	204x204	268
NGC 3136 .....	10 05 47.16	-67 22 26.9	19101119	PHT22	C60	...	181x181	128
	10 05 47.16	-67 22 26.9	19101119	PHT22	C90	...	181x181	64
NGC 3193 .....	10 18 25.49	+21 53 45.4	20200320	PHT22	C60	...	181x181	128
	10 18 25.49	+21 53 45.4	20200320	PHT22	C90	...	181x181	64
	10 18 25.49	+21 53 45.4	20200320	PHT22	C160	...	181x181	64
	10 18 25.49	+21 53 45.4	20200320	PHT22	C200	...	181x181	64
NGC 3250 .....	10 26 32.37	-39 56 42.1	25300221	PHT22	C60	...	181x181	128
	10 26 32.37	-39 56 42.1	25300221	PHT22	C90	...	181x181	64
	10 26 32.37	-39 56 42.1	25300221	PHT22	C160	...	181x181	64
	10 26 32.37	-39 56 42.1	25300221	PHT22	C200	...	181x181	64
NGC 3379 .....	10 47 49.48	+12 34 56.8	22200924	PHT22	C60	...	181x181	128
	10 47 49.48	+12 34 56.8	22200924	PHT22	C90	...	181x181	64
	10 47 49.48	+12 34 56.8	22200924	PHT22	C160	...	181x181	64
	10 47 49.48	+12 34 56.8	22200924	PHT22	C200	...	181x181	64
NGC 3557 .....	11 09 58.38	-37 32 17.2	25401026	PHT22	C60	...	181x181	128
	11 09 58.38	-37 32 17.2	25401026	PHT22	C90	...	181x181	64
	11 09 58.38	-37 32 17.2	25401026	PHT22	C160	...	181x181	64
	11 09 58.38	-37 32 17.2	25401026	PHT22	C200	...	181x181	64
NGC 3610 .....	11 18 25.45	+58 47 11.6	19700428	PHT22	C60	...	181x181	128
	11 18 25.45	+58 47 11.6	19700428	PHT22	C90	...	181x181	64
	11 18 25.45	+58 47 11.6	19700428	PHT22	C160	...	181x181	64
	11 18 25.45	+58 47 11.6	19700428	PHT22	C200	...	181x181	64
NGC 3613 .....	11 18 35.70	+57 59 53.6	20600629	PHT22	C60	...	181x181	128

Table 1—Continued

Name	$\alpha(2000)$	$\delta(2000)$	TDT <sup>a</sup>	AOT <sup>b</sup>	Filter	$N \times M^c$	f.o.v. "×"	$T_{int}^d$ (s)
	11 18 35.70	+57 59 53.6	20600629	PHT22	C90	...	181x181	64
	11 18 35.70	+57 59 53.6	20600629	PHT22	C160	...	181x181	64
	11 18 35.70	+57 59 53.6	20600629	PHT22	C200	...	181x181	64
NGC 3706 .....	11 29 44.03	-36 23 14.9	25401131	PHT22	C60	...	181x181	128
	11 29 44.03	-36 23 14.9	25401131	PHT22	C90	...	181x181	64
	11 29 44.03	-36 23 14.9	25401131	PHT22	C160	...	181x181	64
	11 29 44.03	-36 23 14.9	25401131	PHT22	C200	...	181x181	64
NGC 3904 .....	11 49 13.82	-29 16 35.1	25200832	PHT22	C60	...	181x181	128
	11 49 13.82	-29 16 35.1	25200832	PHT22	C90	...	181x181	64
	11 49 13.82	-29 16 35.1	25200832	PHT22	C160	...	181x181	64
	11 49 13.82	-29 16 35.1	25200832	PHT22	C200	...	181x181	64
NGC 3928 .....	11 51 47.59	+48 41 00.0	15300511	PHT32	C60	4 × 2	411x204	932
	11 51 47.59	+48 41 00.0	15300511	PHT32	C100	4 × 2	411x204	932
	11 51 47.59	+48 41 00.0	16901512	PHT32	C135	4 × 2	457x273	712
	11 51 47.59	+48 41 00.0	16901512	PHT32	C200	4 × 2	457x273	712
	11 51 47.58	+48 40 58.8	15301004	CAM01	LW3	...	210x210	1180
NGC 3962 .....	11 54 40.24	-13 58 29.9	24001933	PHT22	C60	...	181x181	128
	11 54 40.24	-13 58 29.9	24001933	PHT22	C90	...	181x181	64
	11 54 40.24	-13 58 29.9	24001933	PHT22	C160	...	181x181	64
	11 54 40.24	-13 58 29.9	24001933	PHT22	C200	...	181x181	64
NGC 3998 .....	11 57 56.09	+55 27 12.7	14301213	PHT32	C60	4 × 2	411x204	868
	11 57 56.09	+55 27 12.7	14301213	PHT32	C100	4 × 2	411x204	868
	11 57 56.09	+55 27 12.7	14301114	PHT32	C135	4 × 2	457x273	648
	11 57 56.09	+55 27 12.7	14301114	PHT32	C200	4 × 2	457x273	648
	11 57 56.09	+55 27 12.8	19700617	CAM01	LW3	...	216x216	382
NGC 4105 .....	12 06 40.61	-29 45 42.0	57400258	PHT37/39	C60	...	135x135	362
	12 06 40.61	-29 45 42.0	57400258	PHT37/39	C100	...	135x135	362
	12 06 40.61	-29 45 42.0	57400256	PHT37/39	C180	...	181x181	180
	12 06 40.60	-29 45 42.6	57400259	CAM01	LW10	...	204x204	522
NGC 4125 .....	12 08 04.42	+65 10 36.2	19700734	PHT22	C60	...	181x181	128
	12 08 04.42	+65 10 36.2	19700734	PHT22	C90	...	181x181	64
	12 08 04.42	+65 10 36.2	19700734	PHT22	C160	...	181x181	64
	12 08 04.42	+65 10 36.2	19700734	PHT22	C200	...	181x181	64
NGC 4261 .....	12 19 23.19	+05 49 29.7	23900315	PHT22	C60	5 × 2	181x181	1260
	12 19 23.15	+05 49 26.8	22801136	PHT32	C60	...	503x204	128
	12 19 23.15	+05 49 26.8	22801136	PHT22	C90	...	181x181	64
	12 19 23.19	+05 49 29.7	23900315	PHT32	C100	5 × 2	503x204	1260
	12 19 23.19	+05 49 29.7	23900216	PHT32	C135	5 × 2	549x273	1004
	12 19 23.15	+05 49 26.8	22801136	PHT22	C160	...	181x181	64
	12 19 23.19	+05 49 29.7	23900216	PHT22	C200	5 × 2	181x181	1004

Table 1—Continued

Name	$\alpha(2000)$	$\delta(2000)$	TDT <sup>a</sup>	AOT <sup>b</sup>	Filter	$N \times M^c$	f.o.v. "×"	$T_{int}^d$ (s)
	12 19 23.15	+05 49 26.8	22801136	PHT32	C200	...	549x273	64
	12 19 23.17	+05 49 29.4	22801205	CAM01	LW3	...	102x102	420
NGC 4278 .....	12 20 06.63	+29 16 56.8	19800537	PHT22	C60	...	181x181	128
	12 20 06.63	+29 16 56.8	19800537	PHT22	C90	...	181x181	64
	12 20 06.63	+29 16 56.8	19800537	PHT22	C160	...	181x181	64
	12 20 06.63	+29 16 56.8	19800537	PHT22	C200	...	181x181	64
	12 20 06.84	+29 16 49.8	22900605	CAM01	LW3	...	210x210	1280
NGC 4291 .....	12 20 18.10	+75 22 20.2	28800662	PHT37/39	C60	...	135x135	396
	12 20 18.10	+75 22 20.2	28800662	PHT37/39	C100	...	135x135	396
	12 20 18.10	+75 22 20.2	28800664	PHT37/39	C180	...	181x181	244
NGC 4365 .....	12 24 28.80	+07 19 04.8	20201439	PHT22	C60	...	181x181	128
	12 24 28.80	+07 19 04.8	20201439	PHT22	C90	...	181x181	64
	12 24 28.80	+07 19 04.8	20201439	PHT22	C160	...	181x181	64
	12 24 28.80	+07 19 04.8	20201439	PHT22	C200	...	181x181	64
NGC 4374 .....	12 25 03.10	+12 53 10.6	23502141	PHT22	C60	...	181x181	128
	12 25 03.10	+12 53 10.6	23502141	PHT22	C90	...	181x181	64
	12 25 03.10	+12 53 10.6	23502141	PHT22	C160	...	181x181	64
	12 25 03.10	+12 53 10.6	23502141	PHT22	C200	...	181x181	64
	12 25 03.59	+12 53 13.5	23502406	CAM01	LW3	...	210x210	1280
NGC 4472 .....	12 29 46.50	+07 59 57.0	22700701	PHT32	C60	5 × 4	503x342	2140
	12 29 46.50	+07 59 57.0	22700701	PHT32	C90	5 × 4	503x342	2140
	12 29 46.50	+07 59 57.0	22700706	PHT32	C180	5 × 7	549x457	1045
NGC 4473 .....	12 29 48.73	+13 25 49.1	19900447	PHT22	C60	...	181x181	128
	12 29 48.73	+13 25 49.1	19900447	PHT22	C90	...	181x181	64
	12 29 48.73	+13 25 49.1	19900447	PHT22	C160	...	181x181	64
	12 29 48.73	+13 25 49.1	19900447	PHT22	C200	...	181x181	64
NGC 4486 .....	12 30 48.83	+12 23 32.2	22801748	PHT22	C60	...	181x181	128
	12 30 48.83	+12 23 32.2	22801748	PHT22	C90	...	181x181	64
	12 30 48.83	+12 23 32.2	22801748	PHT22	C160	...	181x181	64
	12 30 48.83	+12 23 32.2	22801748	PHT22	C200	...	181x181	64
NGC 4494 .....	12 31 24.47	+25 46 32.2	19800350	PHT22	C60	...	181x181	128
	12 31 24.47	+25 46 32.2	19800350	PHT22	C90	...	181x181	64
	12 31 24.47	+25 46 32.2	19800350	PHT22	C160	...	181x181	64
	12 31 24.47	+25 46 32.2	19800350	PHT22	C200	...	181x181	64
NGC 4552 .....	12 35 39.80	+12 33 23.2	23800621	PHT32	C60	5 × 5	503x503	3192
	12 35 39.80	+12 33 23.2	23800621	PHT32	C100	5 × 5	503x503	3192
	12 35 39.80	+12 33 23.2	23901922	PHT32	C135	5 × 5	549x549	2053
	12 35 39.80	+12 33 23.2	23901922	PHT32	C200	5 × 5	549x549	2053
	12 35 39.80	+12 33 23.5	23902129	CAM01	LW3	...	912x216	532

Table 1—Continued

Name	$\alpha(2000)$	$\delta(2000)$	TDT <sup>a</sup>	AOT <sup>b</sup>	Filter	$N \times M^c$	f.o.v. "×"	$T_{int}^d$ (s)
NGC 4564 .....	12 36 26.65	+11 26 24.0	22802951	PHT22	C60	...	181x181	128
	12 36 26.65	+11 26 24.0	22802951	PHT22	C90	...	181x181	64
	12 36 26.65	+11 26 24.0	22802951	PHT22	C160	...	181x181	64
	12 36 26.65	+11 26 24.0	22802951	PHT22	C200	...	181x181	64
NGC 4589 .....	12 37 24.05	+74 11 30.3	20101352	PHT22	C60	...	181x181	128
	12 37 24.05	+74 11 30.3	20101352	PHT22	C90	...	181x181	64
	12 37 24.05	+74 11 30.3	20101352	PHT22	C160	...	181x181	64
	12 37 24.05	+74 11 30.3	20101352	PHT22	C200	...	181x181	64
NGC 4621 .....	12 42 02.28	+11 38 45.9	23502854	PHT22	C60	...	181x181	128
	12 42 02.28	+11 38 45.9	23502854	PHT22	C90	...	181x181	64
	12 42 02.28	+11 38 45.9	23502854	PHT22	C160	...	181x181	64
	12 42 02.28	+11 38 45.9	23502854	PHT22	C200	...	181x181	64
NGC 4636 .....	12 42 49.72	+02 41 17.2	39600286	PHT37/39	C60	...	135x135	396
	12 42 49.72	+02 41 17.2	39600286	PHT37/39	C100	...	135x135	396
	12 42 49.72	+02 41 17.2	39600288	PHT37/39	C180	...	181x181	244
	12 42 49.83	+02 41 17.3	39600117	CAM01	LW3	...	108x108	834
NGC 4649 .....	12 43 39.68	+11 33 09.0	20201603	PHT32	C60	4 × 4	411x342	1508
	12 43 39.68	+11 33 09.0	20201603	PHT32	C90	4 × 4	411x342	1508
	12 43 39.68	+11 33 09.0	20201605	PHT32	C180	4 × 7	457x365	482
NGC 4660 .....	12 44 32.23	+11 11 11.9	21801556	PHT22	C60	...	181x181	128
	12 44 32.23	+11 11 11.9	21801556	PHT22	C90	...	181x181	64
	12 44 32.23	+11 11 11.9	21801556	PHT22	C160	...	181x181	64
	12 44 32.23	+11 11 11.9	21801556	PHT22	C200	...	181x181	64
NGC 4697 .....	12 48 36.06	-05 48 03.5	21801556	PHT22	C60	...	181x181	128
	12 48 36.06	-05 48 03.5	21801556	PHT22	C90	...	181x181	64
	12 48 36.06	-05 48 03.5	21801556	PHT22	C160	...	181x181	64
	12 48 36.06	-05 48 03.5	21801556	PHT22	C200	...	181x181	64
	12 48 35.79	-05 47 59.9	25701120	PHT32	C200	7 × 1	733x181	467
NGC 5061 .....	13 18 04.80	-26 50 10.8	25201166	PHT22	C60	...	181x181	128
	13 18 04.80	-26 50 10.8	25201166	PHT22	C90	...	181x181	64
	13 18 04.80	-26 50 10.8	25201166	PHT22	C160	...	181x181	64
	13 18 04.80	-26 50 10.8	25201166	PHT22	C200	...	181x181	64
NGC 5084 .....	13 20 16.69	-21 49 37.4	40000126	PHT37/39	C60	...	135x135	328
	13 20 16.69	-21 49 37.4	40000126	PHT37/39	C100	...	135x135	328
	13 20 16.69	-21 49 37.4	40000128	PHT37/39	C180	...	181x181	180
NGC 5173 .....	13 28 25.28	+46 35 29.6	17200725	PHT32	C60	4 × 2	411x204	932
	13 28 25.28	+46 35 29.6	17200725	PHT32	C100	4 × 2	411x204	932
	13 28 25.28	+46 35 29.6	17201426	PHT32	C135	4 × 2	457x273	712

Table 1—Continued

Name	$\alpha(2000)$	$\delta(2000)$	TDT <sup>a</sup>	AOT <sup>b</sup>	Filter	$N \times M^c$	f.o.v. "×"	$T_{int}^d$ (s)
	13 28 25.28	+46 35 29.6	17201426	PHT32	C200	4 × 2	457x273	712
	13 28 25.21	+46 35 29.9	35400412	CAM01	LW3	...	210x210	1280
NGC 5322 .....	13 49 15.31	+60 11 31.6	19701168	PHT22	C60	...	181x181	128
	13 49 15.31	+60 11 31.6	19701168	PHT22	C90	...	181x181	64
	13 49 15.31	+60 11 31.6	19701168	PHT22	C160	...	181x181	64
	13 49 15.31	+60 11 31.6	19701168	PHT22	C200	...	181x181	64
NGC 5353 .....	13 53 26.63	+40 16 57.8	38801132	PHT37/39	C60	...	135x135	360
	13 53 26.63	+40 16 57.8	38801132	PHT37/39	C100	...	135x135	360
	13 53 26.63	+40 16 57.8	38801134	PHT37/39	C180	...	181x181	468
	13 53 26.61	+40 16 58.1	38801135	CAM01	LW10	...	204x204	536
NGC 5363 .....	13 56 07.19	+05 15 17.5	22503324	PHT32	C200	4 × 3	457x365	480
	13 56 06.96	+05 15 19.1	22500814	CAM01	LW3	...	210x210	1280
NGC 5666 .....	14 33 09.40	+10 30 38.2	27000727	PHT32	C60	5 × 5	503x411	1633
	14 33 09.40	+10 30 38.2	27000727	PHT32	C100	5 × 5	503x411	1633
	14 33 09.40	+10 30 38.2	27000828	PHT32	C135	5 × 5	549x549	1503
	14 33 09.40	+10 30 38.2	27000828	PHT32	C200	4 × 2	549x549	1503
	14 33 09.39	+10 30 38.5	27000935	CAM01	LW3	...	216x216	436
NGC 5813 .....	15 01 11.14	+01 42 08.0	62802406	PHT32	C100	8 × 3	555x227	1290
	15 01 11.14	+01 42 08.0	62802307	PHT32	C135	8 × 3	825x365	1168
	15 01 11.14	+01 42 08.0	62802508	PHT32	C180	8 × 3	825x365	1166
NGC 6876 .....	20 18 20.16	-70 51 28.6	29901738	PHT37/39	C60	...	135x135	392
	20 18 20.16	-70 51 28.6	29901738	PHT37/39	C100	...	135x135	392
	20 18 20.16	-70 51 28.6	29901740	PHT37/39	C180	...	181x181	180
NGC 7507 .....	23 12 07.49	-28 32 28.8	19300477	PHT22	C60	...	181x181	128
	23 12 07.49	-28 32 28.8	19300477	PHT22	C90	...	181x181	64
	23 12 07.49	-28 32 28.8	19300477	PHT22	C160	...	181x181	64
	23 12 07.49	-28 32 28.8	19300477	PHT22	C200	...	181x181	64
	23 12 07.58	-28 32 29.1	53700411	CAM01	LW10	...	198x198	170
NGC 7768 .....	23 50 58.42	+27 08 50.3	75800713	PHT32	C60	5 × 5	375x319	1333
IC 1459 .....	22 57 10.45	-36 27 44.5	20002174	PHT22	C60	...	181x181	128
	22 57 10.45	-36 27 44.5	20002174	PHT22	C90	...	181x181	64
	22 57 10.45	-36 27 44.5	20002174	PHT22	C160	...	181x181	64
	22 57 10.45	-36 27 44.5	20002174	PHT22	C200	...	181x181	64
	22 57 10.61	-36 27 44.3	16701036	CAM01	LW3	...	462x216	400

Note. — Units of right ascension are hours, minutes, and seconds; units of declination are degrees, arcminutes, and arcseconds.

<sup>a</sup>Target Dedicated Time identifier (TDT)

<sup>b</sup>Astronomical Observing Template (AOT)

<sup>c</sup>Raster points in Y and Z spacecraft coordinates

<sup>d</sup>On-source integration time

Table 2. Basic Properties of the Sample

Name	D <sup>a</sup> (Mpc)	Log $L_B$ <sup>a</sup> ( $L_{B\odot}$ )	Log $L_X$ <sup>b</sup> ( $ergs^{-1}$ )	$F_{6cm}$ <sup>c</sup> (mJy)	T <sup>d</sup>	type <sup>e</sup>	Log $M_{HI}$ <sup>f</sup> ( $M_\odot$ )	Log $M_{H_2}$ <sup>m</sup> ( $M_\odot$ )	Notes <sup>f</sup>
IC 1459 .....	18.88	10.37	40.71	1016.0	-4.7	E1	$\leq 8.64$	...	d, $eH\alpha$ , R
NGC 0147 .....	0.65	7.92	$\leq 37.45$	12.0	-4.8	dE5	$\leq 6.21$	...	
NGC 0185 .....	0.62	8.07	$\leq 37.36$	...	-4.8	dE3pec	5.10	5.04	
NGC 0221 .....	0.72	8.36	37.77	...	-4.7	E2	$\leq 6.26$	...	
NGC 0596 .....	22.28	10.21	$\leq 39.60$	...	-4.3	E0	8.10 <sup>g</sup>	...	
NGC 0720 .....	20.80	10.38	40.61	...	-4.8	E5	$\leq 8.44$	$\leq 7.77$ <sup>n</sup>	
NGC 0807 .....	64.64	10.39	-	...	-4.8	E	9.92 <sup>h</sup>	9.16 <sup>o</sup>	
NGC 0821 .....	20.99	10.16	$\leq 40.33$	...	-4.8	E6	$\leq 7.96$	...	
NGC 1172 .....	28.71	10.10	$\leq 40.59$	...	-3.9	S01(0,3)	$\leq 9.08$	...	
NGC 1275 .....	70.20	11.22	...	...	-2.2	cDpec	...	9.68	$eH\alpha$ , R, M, possible interaction with N1272
NGC 1332 .....	19.68	10.27	40.53	...	-2.9	S01(6)	8.69	...	physical pair with N1331(E2) at 2.7', d
NGC 1344 .....	18.11	10.30	$\leq 39.48$	...	-3.9	S01(5)	$\leq 9.32$	...	
NGC 1395 .....	20.51	10.44	40.89	2.0	-4.8	E2	...	...	$eH\alpha$
NGC 1553 .....	14.45	10.63	40.52	...	-2.3	S01/2(5)pec	$\leq 8.97$	...	pair with N1549 at 11.5'
NGC 2293 .....	23.92	10.03	$\leq 40.21$	...	-1.1	Sab(s)0+pec	...	...	interacting pair with N2202 at 0.9', d?
NGC 2328 .....	12.20	9.02	$\leq 39.56$	...	-2.9	Sab0-?	8.20 <sup>i</sup>	7.92 <sup>o</sup>	$H\alpha$
NGC 3136 .....	19.11	10.07	$\leq 40.26$	...	-4.8	E4	...	...	d, $eH\alpha$
NGC 3193 .....	21.58	10.15	39.96	...	-4.7	E2	$\leq 7.84$	...	member of a quartet
NGC 3250 .....	37.67	10.71	$\leq 40.65$	...	-4.8	E3	...	...	
NGC 3379 .....	10.00	10.06	$\leq 39.54$	0.8	-4.8	E0	$\leq 6.63$	$\leq 6.65$	d
NGC 3557 .....	32.21	10.76	40.58	270.0	-4.8	E3	$\leq 8.62$	...	d, $eH\alpha$ , R
NGC 3610 .....	27.29	10.40	39.83	50.	-4.2	E5	$\leq 8.63$	...	R, M?
NGC 3613 .....	27.29	10.36	$\leq 40.12$	...	-4.7	E6	$\leq 9.22$	...	
NGC 3706 .....	37.21	10.38	$\leq 41.19$	19.0	-3.3	E4	$\leq 8.77$	...	
NGC 3904 .....	17.86	10.06	$\leq 40.74$	...	-4.6	E2	$\leq 8.31$	...	
NGC 3928 .....	16.11	9.33	-	...	-4.6	Sa(S)b?	8.57 <sup>h</sup>	8.39 <sup>p</sup>	recent starburst
NGC 3962 .....	21.68	10.28	$\leq 40.22$	3.7	-4.8	E1	8.17 <sup>g</sup>	...	d, $eH\alpha$ , R
NGC 3998 .....	17.46	10.08	41.51	92.0	-2.1	S01(3)	8.67	...	$eH\alpha$ , R
NGC 4105 .....	22.85	10.25	40.42	3.7	-4.6	S01/2(3)	...	...	interacting pair with N4106 at 1.2'
NGC 4125 .....	25.94	10.80	40.94	3.0	-4.8	E6	$\leq 8.68$ <sup>h</sup>	7.87 <sup>o</sup>	d, $eH\alpha$ , R
NGC 4261 .....	31.48	10.70	41.21	8300.0	-4.8	E3	...	...	d, $H\alpha$ , R
NGC 4278 .....	16.22	10.24	40.36	351.0	-4.8	E1	8.81	$\leq 8.11$	d, $H\alpha$ , R
NGC 4291 .....	24.55	10.00	40.89	...	-4.8	E3	...	...	
NGC 4365 .....	15.92	10.34	40.25	...	-4.8	E3	$\leq 7.20$	...	$H\alpha$
NGC 4374 .....	15.92	10.57	40.83	2880.0	-4.0	E1	$\leq 8.23$ <sup>h</sup>	$\leq 7.40$ <sup>o</sup>	d, $eH\alpha$ , R
NGC 4472 .....	15.92	10.90	41.43	101.0	-4.7	E1/S01(1)	$\leq 6.90$	7.32 <sup>p</sup>	d, $H\alpha$ , R

Table 2—Continued

Name	D <sup>a</sup> (Mpc)	Log $L_B$ <sup>a</sup> ( $L_{B\odot}$ )	Log $L_X$ <sup>b</sup> ( $ergs^{-1}$ )	$F_{6cm}$ <sup>c</sup> (mJy)	T <sup>d</sup>	type <sup>e</sup>	Log $M_{HI}$ <sup>f</sup> ( $M_\odot$ )	Log $M_{H_2}$ <sup>m</sup> ( $M_\odot$ )	Notes <sup>r</sup>
NGC 4473 .....	16.14	10.15	41.14	...	-4.8	E5	$\leq 7.52$	...	d
NGC 4486 .....	15.92	10.85	42.95	71900.0	-4.3	E0	...	$\leq 8.11$	d, $H\alpha$ , R
NGC 4494 .....	21.28	10.62	$\leq 40.10$	1.0	-4.8	E1	$\leq 7.67$	...	d
NGC 4552 .....	15.92	10.29	40.71	108.0	-4.6	S01(0)	$\leq 7.43$	$\leq 8.71$	d, R
NGC 4564 .....	15.92	9.86	$\leq 39.85$	...	-4.7	E6	$\leq 7.33$	$\leq 8.16$	$H\alpha$
NGC 4589 .....	24.55	10.33	40.36	23.5	-4.8	E2	$\leq 8.70^h$	$\leq 7.98^o$	d, $eH\alpha$ , M, R
NGC 4621 .....	15.92	10.32	40.02	...	-4.8	E5	$\leq 7.73$	$\leq 8.04$	
NGC 4636 .....	15.92	10.51	41.59	45.0	-4.8	E0/S01(6)	$\leq 7.73$	$\leq 9.15$	d, $eH\alpha$ , R
NGC 4649 .....	15.92	10.73	41.28	24.0	-4.6	S01(2)	$\leq 7.93$	7.89	pair with N4647(S)
NGC 4660 .....	15.92	9.74	$\leq 39.39$	...	-4.7	E5	$\leq 7.33$	...	$H\alpha$
NGC 4697 .....	15.14	10.55	40.12	...	-4.8	E6	$\leq 8.90$	7.94 <sup>q</sup>	
NGC 5061 .....	18.28	10.28	39.68	...	-4.3	E0	8.04 <sup>g</sup>	...	
NGC 5084 .....	16.90	10.18	40.49	34.0	-1.6	S01(8)	9.75	$\leq 8.20$	d
NGC 5173 .....	34.99	10.04	$\leq 40.36$	...	-4.9	E0	9.13 <sup>l</sup>	...	
NGC 5322 .....	27.80	10.67	40.21	34.0	-4.8	E4	$\leq 8.51^h$	...	d, $eH\alpha$ , R
NGC 5353 .....	34.67	10.56	41.00	35.0	-2.1	S01(7)/E7	9.70	...	pair with N5354 at 1.2'
NGC 5363 .....	15.79	10.17	40.14	95.0	-0.0	[S03(5)]	8.05	8.48	
NGC 5666 .....	31.12	9.94	-	...	7	S?	9.03 <sup>h</sup>	8.73 <sup>o</sup>	
NGC 5813 .....	26.95	10.53	-	1.7	-4.8	E1	$\leq 8.03$	...	d, $eH\alpha$ , R
NGC 6876 .....	48.56	10.83	41.51	...	-4.9	E3	...	...	pair with N6877 at 82"
NGC 7507 .....	17.78	10.23	$\leq 40.7$	...	-4.8	E0	$\leq 8.10$	...	d
NGC 7768 .....	92.04	10.92	41.74	...	-4.9	cD,E	...	...	

Note. — Luminosities and distances are calculated with  $H_0 = 75 \text{ km s}^{-1} \text{ Mpc}^{-1}$ ; (<sup>a</sup>) data are from the LEDA catalog; (<sup>b</sup>) data are from O’Sullivan et al, 1999; (<sup>c</sup>) “pseudo-6 cm” luminosity from Roberts et al. (1991); (<sup>d</sup>) morphological type code from the LEDA catalog; (<sup>e</sup>) morphological type from the RSA catalog; (<sup>f</sup>) HI data from Roberts et al (1991), unless otherwise indicated; (<sup>g</sup>) from Huchtmeier (1994); (<sup>h</sup>) from Huchtmeier, Sage & Henkel (1995); (<sup>i</sup>) from Sadler et al. (2000); (<sup>l</sup>) from Knapp & Raimond (1984); (<sup>m</sup>) H2 data from Roberts et al (1991), unless otherwise indicated; (<sup>n</sup>) from Braine, Henkel & Wiklind (1997); (<sup>o</sup>) from Wiklind, Combes & Henkel (1995); (<sup>p</sup>) from Lees et al. (1991); (<sup>q</sup>) from Sofue & Wakamatsu (1993); (<sup>r</sup>) d=dust detected through optical extinction;  $H\alpha$ =central emission line gas;  $eH\alpha$ =extended emission lines gas; R=radio source,M=possible recent merger remnant

Table 3. ISO and COBE-DIRBE response to the background

Filter	$\lambda$ ( $\mu\text{m}$ )	PHT 32		PHT 37/39		PHT 22 mini-maps		PHT 22 single-pointing	
		<i>ISO/DIRBE</i>	$\sigma$	<i>ISO/DIRBE</i>	$\sigma$	<i>ISO/DIRBE</i>	$\sigma$	<i>ISO/DIRBE</i>	$\sigma$
C60	60	1.267	0.187	1.030	0.144	1.022	0.042	1.038	0.087
C90	90	1.220	0.097	...	...	0.942	0.055	1.056	0.094
C100	100	1.229	0.167	0.990	0.135	...	...	...	...
C135	150	1.069	0.204	...	...	...	...	...	...
C160	170	...	...	...	...	1.003	0.144	1.049	0.077
C180	180	1.040	0.069	0.934	0.138	...	...	...	...
C200	200	0.932	0.230	...	...	0.832	0.190	0.948	0.167

Note. — *ISO/DIRBE* is the mean ratio of the color-corrected background responses for the two instruments;  $\sigma$  is the standard deviation of the ratios after the ISO backgrounds have been corrected.



Table 4. ISOPHOT P37/39 photometry.

Name	$\lambda$ ( $\mu\text{m}$ )	Flux (Jy)	$\sigma_{Flux}$ (Jy)	$F_{back}$ ( $MJysr^{-1}$ )	$\sigma_{background}$ ( $MJysr^{-1}$ )	Notes
NGC 1332 ....	60	0.49	0.07	8.89	0.72	
	100	1.52	0.04	6.36	0.32	
	180	1.56	0.06	5.45	0.22	
NGC 1553 ....	60	0.74	0.07	6.57	0.50	
	100	1.01	0.04	4.49	0.14	
	180	0.49	0.09	2.42	0.07	
NGC 4105 ....	60	0.61	0.05	9.31	0.58	Interactive System
	100	1.19	0.05	7.46	0.32	
	180	2.21	0.08	6.48	0.21	
NGC 4291 ....	60	$\leq 0.21$	...	7.07	0.61	non detection
	100	$\leq 0.24$	...	5.26	0.37	non detection
	180	$\leq 0.36$	...	4.31	0.36	non detection
NGC 4636 ....	60	0.20	0.08	22.01	2.12	
	100	0.47	0.08	13.43	1.02	
	180	0.79	0.06	6.32	0.32	
NGC 5084 ....	60	1.24	0.09	19.20	1.45	
	100	1.72	0.09	14.42	1.29	
	180	2.68	0.1	11.97	0.97	
NGC 5353 ....	60	0.49	0.05	7.45	0.39	Interactive System
	100	1.44	0.06	4.06	0.31	
	180	2.65	0.09	2.07	0.09	
NGC 6876 ....	60	$\leq 0.21$	...	8.64	0.76	non detection
	100	$\leq 0.21$	...	6.66	0.56	non detection
	180	$\leq 0.33$	...	5.74	0.44	non detection

Table 5. ISOPHOT PHT 22 *single-pointing* photometry.

Name	$\lambda$ ( $\mu\text{m}$ )	Flux (Jy)	$\sigma_{Flux}$ (Jy)	$F_{back}$ ( $MJysr^{-1}$ )	$\sigma_{background}$ ( $MJysr^{-1}$ )	Notes
NGC 3136 ....	60	$\leq 0.24$	...	8.96	0.28	non detection
	90	$\leq 0.27$	...	13.28	0.54	non detection
NGC 3193 ....	60	$\leq 0.29$	...	19.45	0.67	non detection
	90	$\leq 0.26$	...	12.31	0.43	non detection
	170	$\leq 0.34$	...	6.00	0.19	non detection
	200	$\leq 0.35$	...	4.06	0.22	non detection
NGC 3250 ....	60	$\leq 0.32$	...	8.99	0.18	non detection
	90	$\leq 0.35$	...	8.90	0.28	non detection
NGC 3379 ....	60	$\leq 0.33$	...	27.22	0.64	non detection
	90	$\leq 0.28$	...	16.60	0.57	non detection
	170	$\leq 0.42$	...	7.66	0.32	non detection
	200	$\leq 0.45$	...	5.65	0.34	non detection
NGC 3557 ....	60	0.29	0.10	12.22	0.39	
	90	0.38	0.09	11.18	0.46	
NGC 3610 ....	60	$\leq 0.35$	...	8.26	0.27	non detection
	90	$\leq 0.27$	...	5.22	0.21	non detection
	170	$\leq 0.32$	...	3.18	0.19	non detection
	200	$\leq 0.41$	...	1.56	0.18	non detection
NGC 3613 ....	60	$\leq 0.28$	...	14.50	0.34	non detection
	90	$\leq 0.28$	...	9.72	0.26	non detection
	170	$\leq 0.34$	...	6.09	0.20	non detection
	200	$\leq 0.42$	...	5.51	0.17	non detection
NGC 3706 ....	60	$\leq 0.29$	...	10.45	0.38	non detection
	90	$\leq 0.21$	...	9.32	0.35	non detection
NGC 3904 ....	60	$\leq 0.30$	...	12.31	0.29	non detection
	90	$\leq 0.21$	...	9.57	0.32	non detection
	170	$\leq 0.38$	...	8.27	0.28	non detection
	200	$\leq 0.37$	...	6.74	0.23	non detection
NGC 3962 ....	60	0.44	0.11	17.25	0.55	
	90	0.54	0.09	11.84	0.57	
	170	0.81	0.13	7.43	0.34	
	200	0.51	0.16	5.75	0.28	
NGC 4125 ....	60	0.69	0.12	7.23	0.41	
	90	1.03	0.11	5.15	0.45	
	170	1.64	0.12	3.50	0.21	
	200	1.24	0.13	2.78	0.19	
NGC 4261 ....	60	0.07	0.08	21.34	0.86	

Table 5—Continued

Name	$\lambda$ ( $\mu\text{m}$ )	Flux (Jy)	$\sigma_{Flux}$ (Jy)	$F_{back}$ ( $MJysr^{-1}$ )	$\sigma_{background}$ ( $MJysr^{-1}$ )	Notes
	90	0.16	0.08	13.81	0.68	
	170	0.39	0.11	6.38	0.32	
	200	0.31	0.10	4.71	0.23	
NGC 4278 ....	60	0.62	0.16	12.52	0.65	
	90	1.24	0.14	9.41	0.58	
	170	2.24	0.18	5.12	0.42	
	200	1.45	0.19	4.63	0.37	
NGC 4365 ....	60	$\leq 0.26$	...	14.50	0.39	non detection
	90	$\leq 0.28$	...	9.72	0.27	non detection
	170	$\leq 0.37$	...	6.09	0.24	non detection
	200	$\leq 0.39$	...	5.50	0.21	non detection
NGC 4374 ....	60	0.41	0.09	19.61	0.67	
	90	0.66	0.11	12.02	0.58	
	170	0.71	0.13	7.18	0.34	
	200	0.49	0.12	5.57	0.29	
NGC 4473 ....	60	$\leq 0.32$	...	14.10	0.32	non detection
	90	$\leq 0.29$	...	9.33	0.30	non detection
	170	$\leq 0.32$	...	5.31	0.28	non detection
	200	$\leq 0.34$	...	4.17	0.23	non detection
NGC 4486 ....	60	$\leq 0.30$	...	18.74	0.39	non detection
	90	$\leq 0.32$	...	12.61	0.41	non detection
	170	$\leq 0.35$	...	5.22	0.29	non detection
	200	$\leq 0.38$	...	4.21	0.25	non detection
NGC 4494 ....	60	0.31	0.08	11.24	0.36	
	90	0.51	0.08	7.67	0.39	
	170	0.74	0.12	4.57	0.21	
	200	0.39	0.15	5.02	0.23	
NGC 4564 ....	60	$\leq 0.24$	...	15.57	0.34	non detection
	90	$\leq 0.28$	...	10.67	0.32	non detection
	170	$\leq 0.36$	...	5.96	0.23	non detection
	200	$\leq 0.42$	...	5.18	0.19	non detection
NGC 4589 ....	60	0.21	0.10	7.88	0.27	
	90	0.31	0.12	6.15	0.31	
	170	0.63	0.16	4.17	0.21	
	200	0.51	0.20	3.78	0.19	
NGC 4621 ....	60	$\leq 0.26$	...	15.48	0.37	non detection
	90	$\leq 0.27$	...	10.38	0.29	non detection
	170	$\leq 0.36$	...	5.81	0.21	non detection
	200	$\leq 0.38$	...	3.98	0.19	non detection

Table 5—Continued

Name	$\lambda$ ( $\mu\text{m}$ )	Flux (Jy)	$\sigma_{Flux}$ (Jy)	$F_{back}$ ( $MJysr^{-1}$ )	$\sigma_{background}$ ( $MJysr^{-1}$ )	Notes
NGC 4660 ....	60	$\leq 0.21$	...	14.43	0.41	non detection
	90	$\leq 0.26$	...	10.13	0.38	non detection
	170	$\leq 0.35$	...	5.87	0.26	non detection
	200	$\leq 0.42$	...	5.42	0.27	non detection
NGC 4697 ....	60	0.48	0.08	27.01	1.10	
	90	0.82	0.08	17.32	0.93	
	170	0.88	0.12	8.33	0.36	
	200	0.62	0.12	7.36	0.32	
NGC 5061 ....	60	$\leq 0.30$	...	15.24	0.41	non detection
	90	$\leq 0.32$	...	11.60	0.38	non detection
	170	$\leq 0.39$	...	10.51	0.39	non detection
	200	$\leq 0.41$	...	9.69	0.41	non detection
NGC 5322 ....	60	0.46	0.10	6.28	0.31	
	90	0.65	0.11	5.03	0.42	
	170	0.61	0.13	3.32	0.35	
	200	0.44	0.15	2.91	0.25	
NGC 7507 ....	60	0.22	0.10	13.46	0.94	
	90	0.31	0.10	9.95	0.84	
	170	0.70	0.18	6.96	0.68	
	200	0.55	0.19	4.94	0.61	
IC 1459 ....	60	0.52	0.12	11.89	0.54	
	90	0.58	0.09	8.54	0.43	
	170	1.12	0.18	4.37	0.28	
	200	0.74	0.20	3.62	0.21	

Table 6. ISOPHOT PHT 22 *Mini-map* photometry.

Name	$\lambda$ ( $\mu\text{m}$ )	Flux (Jy)	$\sigma_{Flux}$ (Jy)	$F_{back}$ ( $MJysr^{-1}$ )	$\sigma_{background}$ ( $MJysr^{-1}$ )	Notes
NGC 147 ....	60	$\leq 0.06$	...	9.97	0.30	non detection
	90	$\leq 0.09$	...	10.01	0.18	non detection
	170	$\leq 0.21$	...	15.34	0.61	non detection
	200	$\leq 0.21$	...	12.63	0.25	non detection
NGC 185 ....	60	0.28	0.04	10.97	0.33	
	90	0.92	0.03	13.24	0.42	
	170	1.61	0.21	16.37	0.49	
	200	1.01	0.12	13.22	0.26	
NGC 221 ....	60	$\leq 0.06$	...	12.11	0.49	non detection
	90	$\leq 0.06$	...	10.41	0.29	non detection
	170	$\leq 0.24$	...	16.10	1.30	non detection
	200	$\leq 0.27$	...	13.14	1.34	non detection
NGC 596 ....	60	$\leq 0.09$	...	16.35	0.63	non detection
	90	$\leq 0.06$	...	10.31	0.18	non detection
	170	$\leq 0.12$	...	6.04	0.35	non detection
	200	$\leq 0.27$	...	4.22	0.14	non detection
NGC 720 ....	60	$\leq 0.09$	...	12.94	0.42	non detection
	90	$\leq 0.06$	...	7.86	0.15	non detection
	170	$\leq 0.09$	...	3.92	0.27	non detection
	200	$\leq 0.12$	...	2.24	0.09	non detection
NGC 821 ....	60	$\leq 0.12$	...	26.11	0.78	non detection
	90	$\leq 0.06$	...	16.94	0.22	non detection
	170	$\leq 0.24$	...	12.66	0.56	non detection
	200	$\leq 0.30$	...	9.43	0.36	non detection
NGC 1275 ....	170	4.45	0.18	15.92	0.75	
	200	2.92	0.14	11.78	0.08	
NGC 1395 ....	60	0.08	0.03	8.89	0.31	
	90	0.18	0.03	5.73	0.07	
	170	0.24	0.05	5.46	0.34	
	200	0.20	0.04	4.13	0.11	

Table 7. ISOPHOT P32 photometry.

Name	$\lambda$ ( $\mu\text{m}$ )	$F_{model}^a$ (Jy)	$F_{map}^b$ (Jy)	$\sigma_{map}$ (Jy)	$F_{back}^c$ ( $MJysr^{-1}$ )	$\sigma_{background}$ ( $MJysr^{-1}$ )	Notes <sup>d</sup>
NGC 0807 ....	150	2.53	2.67	0.09	13.18	0.43	beam-fit
NGC 1172 ....	150	$\leq 0.19$	$\leq 0.24$	...	9.62	0.41	non detection
	200	$\leq 0.21$	$\leq 0.27$	...	9.44	0.32	non detection
NGC 1344 ....	60	$\leq 0.10$	$\leq 0.12$	...	9.02	0.54	non detection
	90	$\leq 0.09$	$\leq 0.09$	...	6.71	0.46	non detection
	180	$\leq 0.12$	$\leq 0.09$	...	3.25	0.27	non detection
NGC 2293 ....	60	$\leq 0.14$	$\leq 0.12$	...	11.82	0.71	non detection
	100	$\leq 0.21$	$\leq 0.21$	...	16.26	1.46	non detection
	200	...	3.01	0.17	11.16	0.44	Interactive System
NGC 2328 ....	150	2.64	2.68	0.07	12.20	0.36	beam-fit
NGC 3928 ....	60	2.62	2.87	0.11	12.27	0.98	beam-fit
	100	3.32	3.15	0.11	6.65	0.59	beam-fit
	150	3.69	3.88	0.15	5.77	0.40	beam-fit
	200	2.99	2.96	0.09	2.88	0.23	beam-fit
NGC 3998 ....	60	0.35	0.46	0.04	14.21	1.01	beam-fit
	100	0.57	0.61	0.03	8.44	0.67	beam-fit
	150	0.75	0.77	0.08	4.65	0.19	beam-fit
	200	0.27	0.51	0.04	2.77	0.16	beam-fit
NGC 4261 ....	60	$\leq 0.10$	0.05	0.02	20.21	1.41	
	100	0.25	0.21	0.04	11.57	0.81	Extended
	150	0.28	0.35	0.02	4.26	0.13	Extended
	200	0.16	0.21	0.03	2.32	0.23	beam-fit
NGC 4472 ....	60	$\leq 0.13$	$\leq 0.12$	...	21.11	1.05	non detection
	90	$\leq 0.12$	$\leq 0.12$	...	13.17	0.65	non detection
	180	$\leq 0.10$	$\leq 0.09$	...	5.54	0.26	non detection
NGC 4552 ....	60	$\leq 0.14$	$\leq 0.18$	...	18.51	0.83	non detection
	100	$\leq 0.15$	0.17	0.04	9.74	0.41	
	150	0.16	0.13	0.02	7.12	0.23	beam-fit
	200	$\leq 0.11$	0.10	0.03	4.38	0.16	
NGC 4649 ....	60	$\leq 0.13$	$\leq 0.13$	...	15.44	0.86	non detection
	90	$\leq 0.11$	$\leq 0.12$	...	10.39	0.56	non detection
	180	$\leq 0.12$	$\leq 0.10$	...	5.54	0.32	non detection
NGC 5173 ....	60	0.31	0.33	0.04	12.23	0.76	Extended
	100	0.46	0.45	0.03	8.38	0.35	Extended
	150	0.82	0.87	0.04	6.38	0.27	Extended
	200	0.64	0.71	0.04	3.89	0.20	Extended

Table 7—Continued

Name	$\lambda$ ( $\mu\text{m}$ )	$F_{model}^a$ (Jy)	$F_{map}^b$ (Jy)	$\sigma_{map}$ (Jy)	$F_{back}^c$ ( $MJysr^{-1}$ )	$\sigma_{background}$ ( $MJysr^{-1}$ )	Notes <sup>d</sup>
NGC 5363 ....	200	3.02	3.32	0.09	5.10	0.32	Extended
NGC 5666 ....	60	1.78	1.69	0.05	16.13	0.82	beam-fit
	100	2.81	3.11	0.05	10.67	0.62	Extended
	150	3.31	3.91	0.11	7.45	0.24	Extended
	200	2.04	2.68	0.06	2.91	0.18	Extended <sup>e</sup>
NGC 5813 ....	100	0.12	0.11	0.03	9.49	0.30	beam-fit
	150	$\leq 0.16$	$\leq 0.18$	...	7.73	0.23	non detection
	200	$\leq 0.22$	$\leq 0.21$	...	6.71	0.22	non detection
NGC 7768 ....	60	$\leq 0.15$	$\leq 0.12$	...	12.25	0.52	non detection

<sup>a</sup>The flux derived from a model fit to the data; For the nondetections the upper limits are indicated as the flux densities to the  $3\sigma$  uncertainties in the amplitude of the psf-fit model.

<sup>b</sup>The flux density derived from direct integration of the reduced maps

<sup>c</sup>The average background brightness

<sup>d</sup>Beam-fit indicates that a beam model has been used to extract the photometry for pointlike sources.

<sup>e</sup>The  $F_{model}$  flux is a lower limit to the true flux, since our fit model it is not an appropriate fit for the source.

Table 8. ISOCAM Mid-infrared photometry

Name	$\lambda_{\text{ref}}$ ( $\mu\text{m}$ )	$\delta\lambda$ ( $\mu\text{m}$ )	Flux (mJy)	$\sigma$ (mJy)
NGC 185.....	14.3	5	53.8	8.1
NGC 1275 ...	14.3	5	221.4	26.5
NGC 1332 ...	12.0	6	126.6	21.1
NGC 1395 ...	14.9	2	37.0	16.2
NGC 1553 ...	12.0	6	162.3	29.2
NGC 2328 ...	14.3	5	84.3	12.6
NGC 3928 ...	14.3	5	165.7	32.8
NGC 3998 ...	14.3	5	103.7	19.6
NGC 4105 ...	12.0	6	114.9	24.1
NGC 4261 ...	14.3	5	98.4	17.7
NGC 4278 ...	12.0	6	56.2	15.3
NGC 4374 ...	12.0	6	72.6	27.6
NGC 4552 ...	14.3	5	58.7	22.3
NGC 4636 ...	14.3	5	131.4	26.3
NGC 5084 <sup>a</sup> ...	12.0	6	159.0	...
NGC 5813 <sup>a</sup> ...	12.0	6	151.0	...
NGC 5173 ...	12.0	6	27.3	16.4
NGC 5353 ...	12.0	6	74.2	19.4
NGC 5363 ...	12.0	6	86.4	21.2
NGC 5666 ...	14.3	5	86.5	26.9
NGC 7507 ...	14.9	2	73.6	21.9
IC 1459 .....	14.3	5	65.5	16.4

<sup>a</sup>Photometry is from Ferrari et al. (2002).



Table 9. Dust Temperatures and Masses

Name	Single-Blackbody Model, $\beta$ variable				Single-Blackbody Model, $\beta=2$			Two-Blackbody Model, $\beta=2$			
	reduced $\chi^2$	$\beta$	$T_D$ (K)	$M_D$ ( $\times 10^4 M_\odot$ )	reduced $\chi^2$	$T_D$ (K)	$M_D$ ( $\times 10^4 M_\odot$ )	$T_D^{warm}$ (K)	$M_D^{warm}$ ( $\times 10^4 M_\odot$ )	$T_D^{cold}$ (K)	$M_D^{cold}$ ( $\times 10^4 M_\odot$ )
NGC 0147 .....	...	...	...	...	...	...	...	...	...	20	$\leq 0.041$
NGC 0185 .....	1.8	1.2	26	0.039	1.9	22	0.15	42	0.00023	21	0.16
NGC 0221 .....	...	...	...	...	...	...	...	...	...	20	$\leq 0.065$
NGC 0596 .....	...	...	...	...	...	...	...	...	...	20	$\leq 62$
NGC 0720 .....	...	...	...	...	...	...	...	...	...	20	$\leq 24$
NGC 0807 .....	...	1.0	25	690	7.4	20	3840	43	12	19	5270
NGC 0821 .....	...	...	...	...	...	...	...	...	...	20	$\leq 61$
NGC 1172 .....	...	...	...	...	...	...	...	...	...	20	$\leq 99$
NGC 1275 .....	19.7	1.0	43	250	32	34	1310	46	150	21	4510
NGC 1332 .....	...	1.4	26	48	4.7	23	150	43	0.68	22	170
NGC 1344 .....	...	...	...	...	...	...	...	...	...	20	$\leq 14$
NGC 1395 .....	0.27	1.2	26	6.1	0.82	22	26	44	0.12	20	35
NGC 1553 .....	...	1.8	33	6.1	0.21	32	8.8	43	0.32	30	9.5
NGC 2293 .....	...	...	...	...	...	...	...	...	...	...	...
NGC 2328 .....	...	1.0	37	7.7	10	31	27	43	2.0	24	49
NGC 3136 .....	...	...	...	...	...	...	...	...	...	...	...
NGC 3193 .....	...	...	...	...	...	...	...	...	...	20	$\leq 73$
NGC 3250 .....	...	...	...	...	...	...	...	...	...	...	...
NGC 3379 .....	...	...	...	...	...	...	...	...	...	20	$\leq 19$
NGC 3557 .....	...	...	...	...	...	...	...	...	...	...	...
NGC 3610 .....	...	...	...	...	...	...	...	...	...	20	$\leq 140$
NGC 3613 .....	...	...	...	...	...	...	...	...	...	20	$\leq 140$
NGC 3706 .....	...	...	...	...	...	...	...	...	...	...	...
NGC 3904 .....	...	...	...	...	...	...	...	...	...	20	$\leq 56$
NGC 3928 .....	62	1.0	33	21	110	27	120	43	5.4	18	470
NGC 3962 .....	4.3	1.0	31	10	3.6	25	63	46	0.94	20	120
NGC 3998 .....	19	1.0	32	6.1	18	26	28	47	0.56	20	65
NGC 4105 .....	...	1.0	23	115	64	19	559	43	2.2	17	930
NGC 4125 .....	7.1	1.0	27	59	5.3	23	254	47	1.8	20	410
NGC 4261 .....	0.21	1.3	22	43	0.42	20	154	33	1.6	18	210
NGC 4278 .....	4.6	1.0	27	25	2.4	22	152	42	0.93	20	185
NGC 4291 .....	...	...	...	...	...	...	...	...	...	20	$\leq 100$
NGC 4365 .....	...	...	...	...	...	...	...	...	...	20	$\leq 46$
NGC 4374 .....	1.0	1.3	30	8.0	1.9	26	25	42	0.68	22	37

Table 9—Continued

Name	Single-Blackbody Model, $\beta$ variable				Single-Blackbody Model, $\beta=2$			Two-Blackbody Model, $\beta=2$			
	reduced $\chi^2$	$\beta$	$T_D$ (K)	$M_D$ ( $\times 10^4 M_\odot$ )	reduced $\chi^2$	$T_D$ (K)	$M_D$ ( $\times 10^4 M_\odot$ )	$T_D^{warm}$ (K)	$M_D^{warm}$ ( $\times 10^4 M_\odot$ )	$T_D^{cold}$ (K)	$M_D^{cold}$ ( $\times 10^4 M_\odot$ )
NGC 4472 .....	...	...	...	...	...	...	...	...	...	20	$\leq 11$
NGC 4473 .....	...	...	...	...	...	...	...	...	...	20	$\leq 41$
NGC 4486 .....	...	...	...	...	...	...	...	...	...	20	$\leq 44$
NGC 4494 .....	3.4	1.1	30	14	1.9	25	51	42	0.83	22	74
NGC 4552 .....	1.1	2.0	28	3.4	0.8	28	3.4	38	0.39	24	4.2
NGC 4564 .....	...	...	...	...	...	...	...	...	...	20	$\leq 44$
NGC 4589 .....	4.0	1.3	22	42	1.8	21	112	43	0.85	18	220
NGC 4621 .....	...	...	...	...	...	...	...	...	...	20	$\leq 43$
NGC 4636 .....	...	1.2	23	21	3.0	19	91	43	0.33	18 130	
NGC 4649 .....	...	...	...	...	...	...	...	...	...	20	$\leq 11$
NGC 4660 .....	...	...	...	...	...	...	...	...	...	20	$\leq 47$
NGC 4697 .....	1.2	1.3	30	8.6	1.8	26	27	40	1.0	22	42
NGC 5061 .....	...	...	...	...	...	...	...	...	...	20	$\leq 62$
NGC 5084 .....	...	1.0	24	55	68	21	260	43	2.5	17	600
NGC 5173 .....	26	1.0	23	86	19	19	440	48	1.6	17	750
NGC 5322 .....	1.5	1.3	32	16	1.6	28	50	42	2.5	22	93
NGC 5353 .....	...	1.0	23	240	42	19	1580	43	3.6	18	2160
NGC 5363 .....	...	1.6	27	92.8	2.5	25	180	43	0.81	24	200
NGC 5666 .....	45	1.0	30	100	87	25	520	41	14	21	1010
NGC 5813 .....	...	...	...	...	...	...	...	...	...	20	$\leq 70$
NGC 6876 .....	...	...	...	...	...	...	...	...	...	20	$\leq 360$
NGC 7507 .....	3.8	1.2	24	17	1.8	20	75	46	0.34	18	130
NGC 7768 .....	...	...	...	...	...	...	...	...	...	...	...
IC 1459 .....	7.4	1.1	26	23	4.4	22	100	48	0.67	19	180

Note. — The estimated errors on the derived temperatures are  $\sim 10\%$ .

Table 10. FIR angular extent

Name	$R_e$ <sup>a</sup> arcsec	$\lambda$ ( $\mu\text{m}$ )	S <sup>b</sup> ( $MJysr^{-1}$ )	$\sigma_{T,major}$ <sup>c</sup> (arcsec)	$\sigma_{S,major}$ <sup>d</sup> (arcsec)	$\sigma_{T,minor}$ <sup>c</sup> (arcsec)	$\sigma_{S,minor}$ <sup>d</sup> (arcsec)	P.A. <sup>e</sup> degree
NGC 4261 ....	38.6	100	3.62	37.5	32.5	22.1	11.9	1
		150	1.12	60.7	46.0	42.2	13.7	59
NGC 5173 ....	14.1	60	5.29	25.1	16.8	20.1	7.6	-51
		100	6.58	25.3	14.9	20.9	4.5	9
		150	2.93	48.7	27.8	40.3	5.7	-75
		200	1.98	49.0	26.7	44.8	17.8	-76
NGC 5363 ....	39.1	200	5.17	66.2	51.9	47.7	24.2	73
NGC 5666 ....	13.4	100	22.76	23.7	12.1	22.6	9.7	90
		150	5.75	68.2	55.3	41.3	10.7	89
		200	2.62	70.5	57.3	54.1	35.2	84

<sup>a</sup>Optical effective radii are from Faber et al. (1989). For those galaxies not included in their list,  $R_e$  has been derived from the linear relation between  $\log R_e$  and  $M_v$  presented in Faber et al. (1997), assuming  $B - V = 1$ .

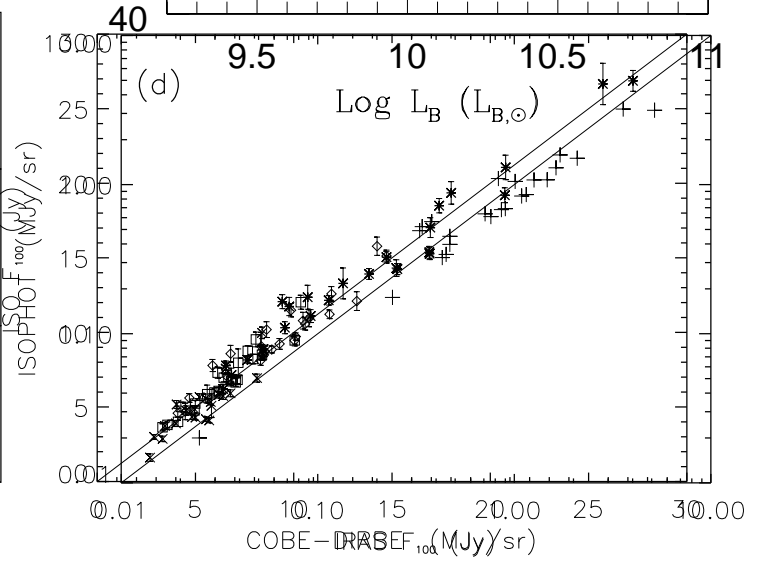
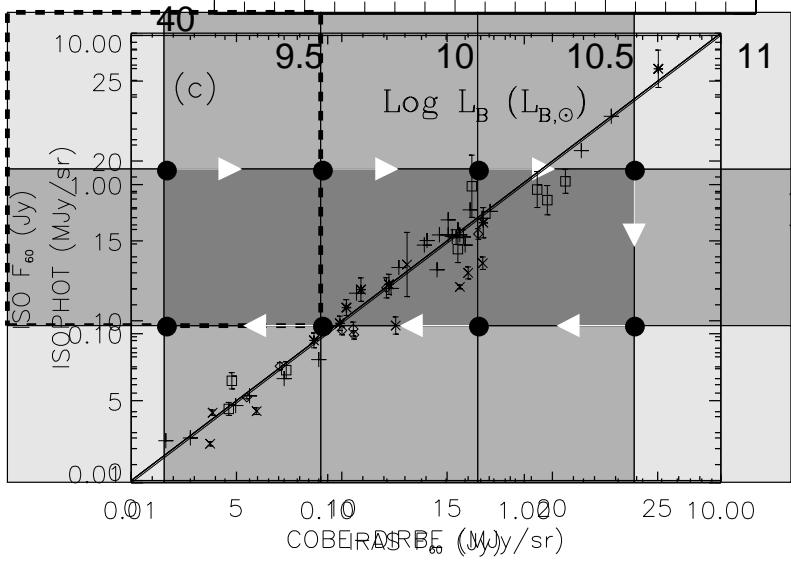
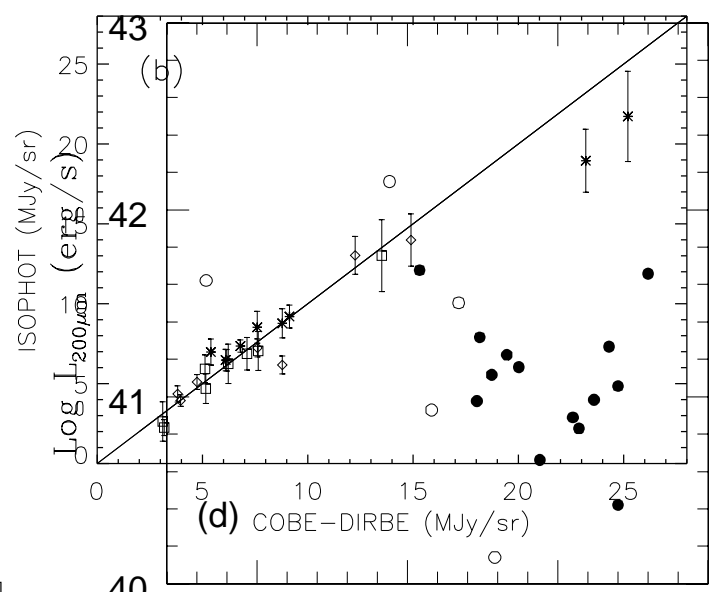
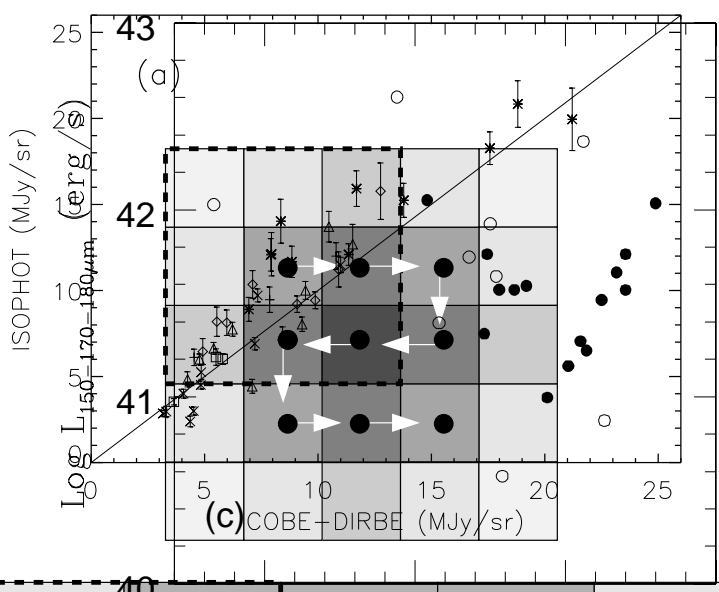
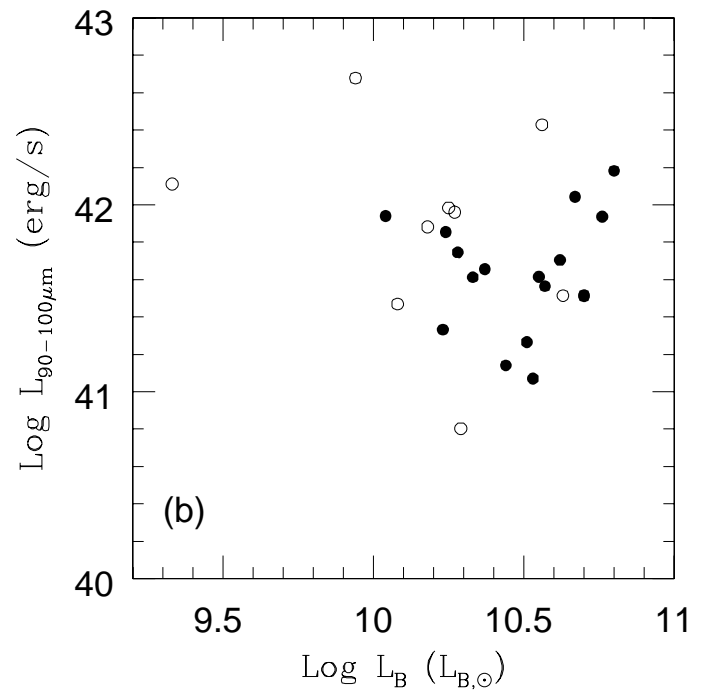
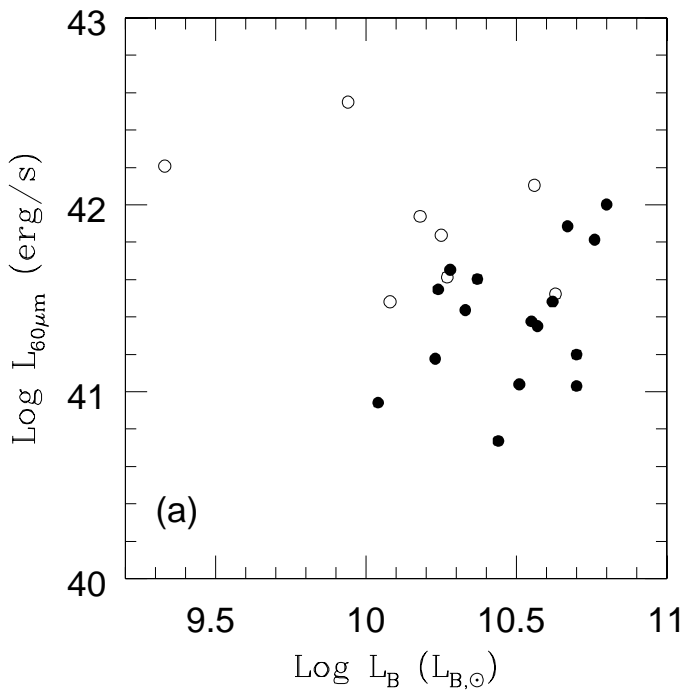
<sup>b</sup>The amplitude S of the source model.

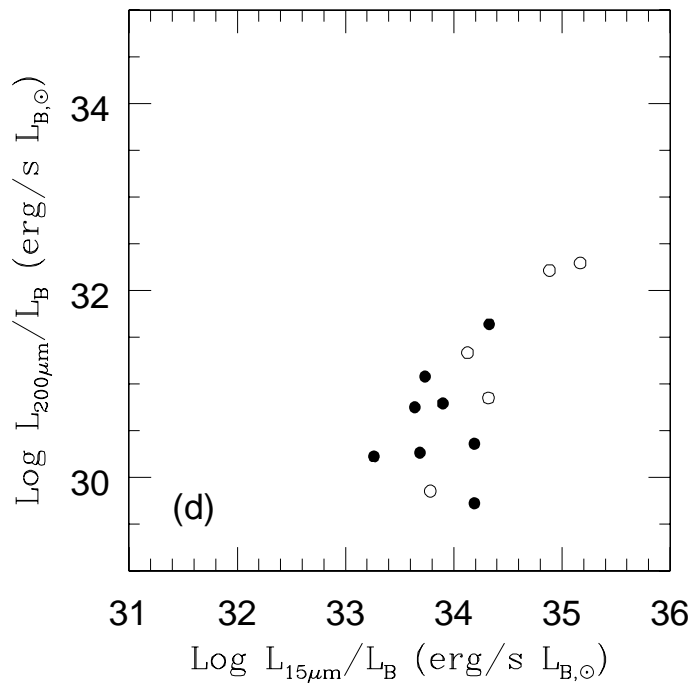
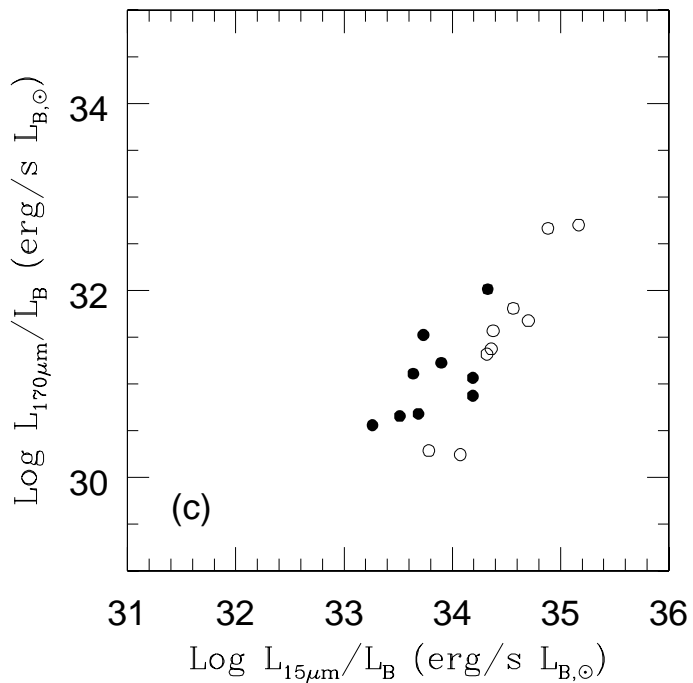
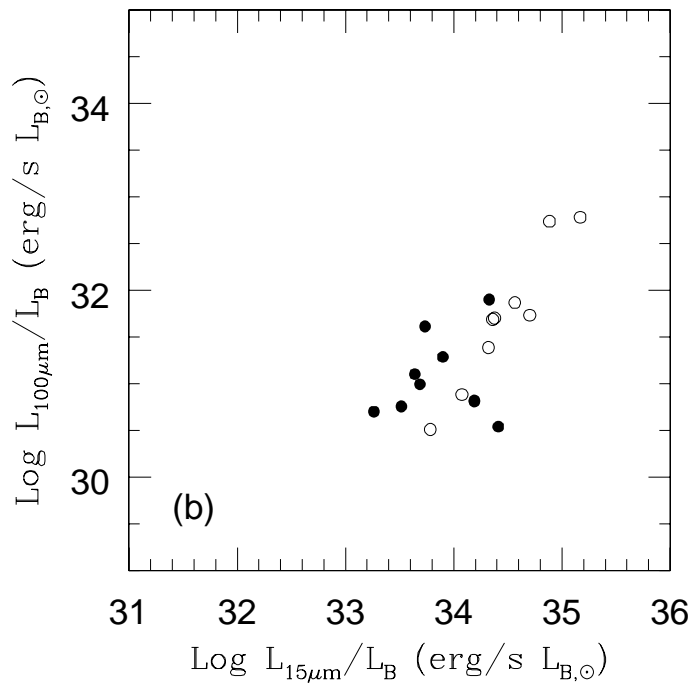
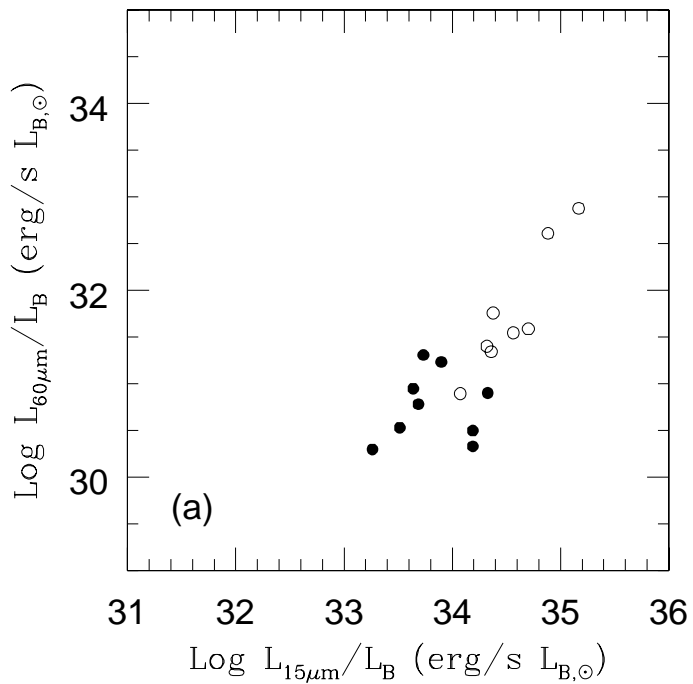
<sup>c</sup>The width  $\sigma_{T,major}$  ( $\sigma_{T,minor}$ ) in arcsec of the major (minor) axis of the fitted elliptical gaussian. The FWHM is  $2.354\sigma_{T,major}$

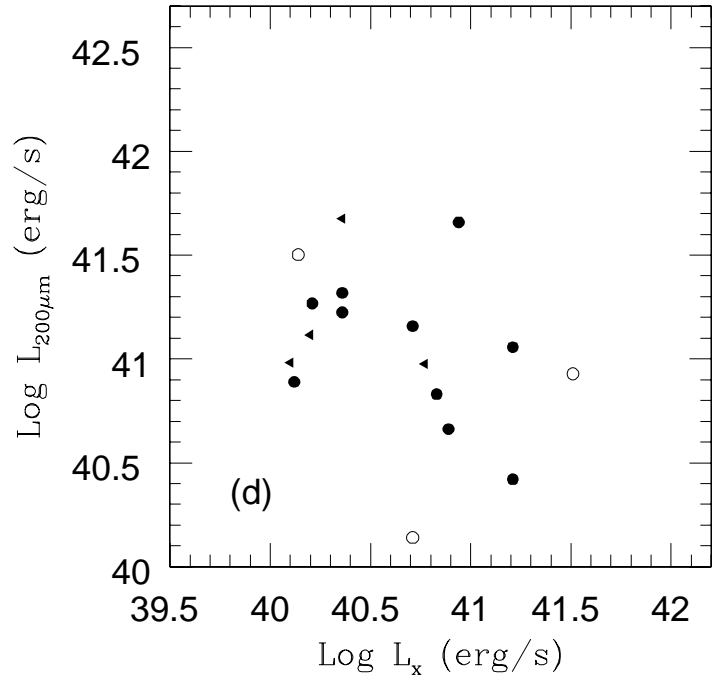
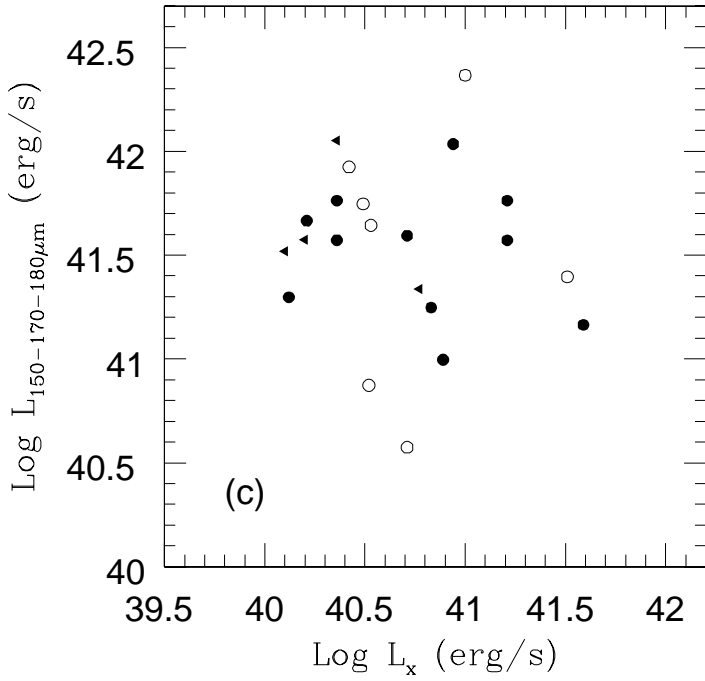
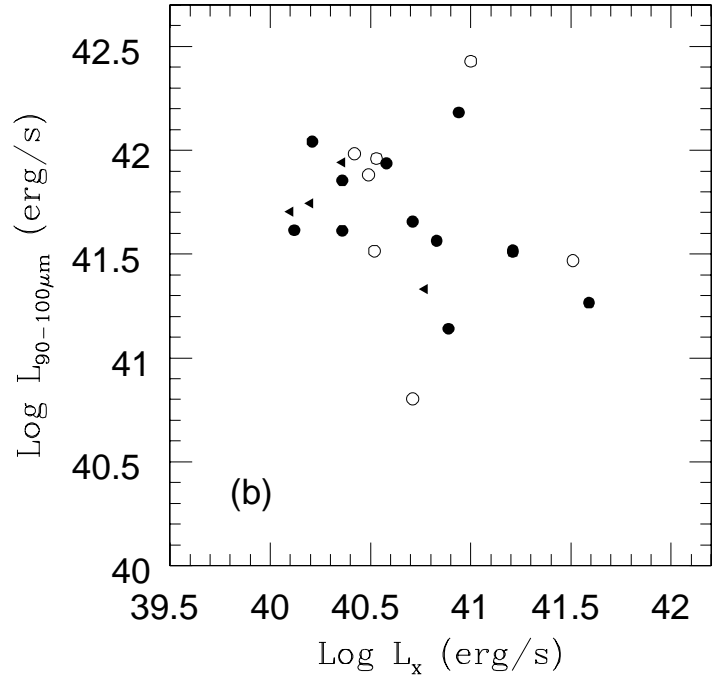
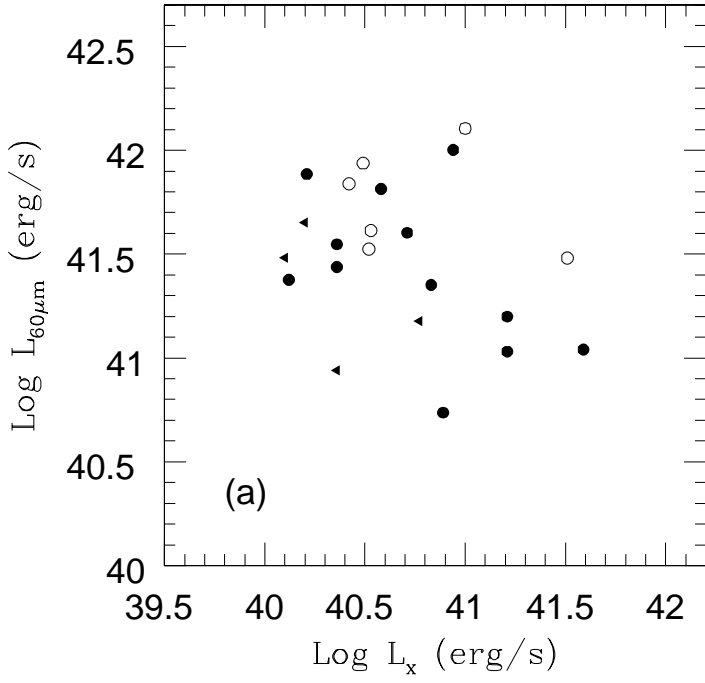
<sup>d</sup>The width  $\sigma_{S,major}$  ( $\sigma_{S,minor}$ ) in arcsec of the major (minor) axis of the gaussian source model.

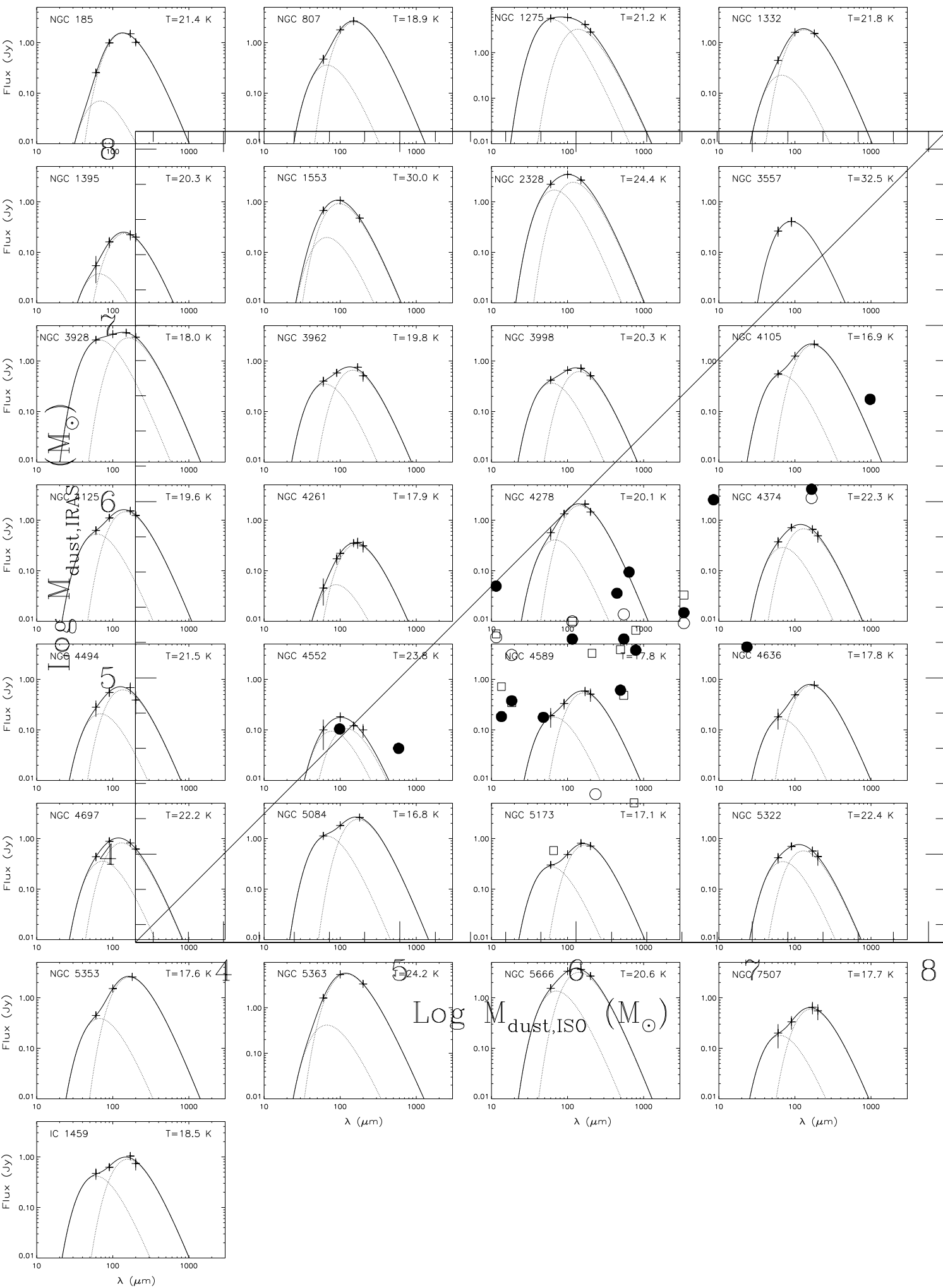
<sup>e</sup>The Position Angle P.A. of the two-dimensional fitted gaussian. The position angle is defined as the rotation of the ellipse from the scan direction axis (y-axis) clockwise.

Note. — NGC 5666 at 200  $\mu\text{m}$  has a complex surface brightness; our simple two-dimensional gaussian fit has to be considered as a tentative fit. A multi-component fit would be more appropriate to describe the light profile at this wavelength.









This figure "f9a.png" is available in "png" format from:

<http://arxiv.org/ps/astro-ph/0312248v1>



This figure "f9b.png" is available in "png" format from:

<http://arxiv.org/ps/astro-ph/0312248v1>

This figure "f9c.png" is available in "png" format from:

<http://arxiv.org/ps/astro-ph/0312248v1>

This figure "f9d.png" is available in "png" format from:

<http://arxiv.org/ps/astro-ph/0312248v1>